ANALYSIS OF SPOT PATTERNS ON A COORDINATE-INVARIANT MODEL FOR VEGETATION ON A CURVED TERRAIN

J. C. TZOU*, L. TZOU†

Abstract. Motivated by the model proposed by Gandhi et al. in [J. R. Soc. Interface **15**, 20180508], we propose a two-component reaction-advection-diffusion model for vegetation density and soil water concentration on a curved terrain with elevation given by $z = \zeta(x, y)$ and metric tensor $g(x, y)$. It accounts for downhill flow of soil water, spatially dependent effective evaporation of soil water, and vertical rainfall on a curved surface. In the singularly perturbed limit of slow vegetation diffusion $0 < \varepsilon^2 \ll 1$, we use a hybrid asymptotic-numerical method to construct a localized quasi-equilibrium one-spot solution corresponding to one spot of a spotted vegetation pattern. We derive an ODE for the slow motion of the spot, finding that it is governed by three factors that arise at two different orders in ε. The leading order $\mathcal{O}(\varepsilon^2|\log\varepsilon|)$ effects are that of soil water advection and effective evaporation rate, the first driving the spot uphill while the second drive it toward regions of slow effective evaporation (e.g., valleys). Entering at $\mathcal{O}(\varepsilon^2)$ are effects due to surface curvature along with higher order contributions of advection and variable evaporation rate. The combined effect of these three factors is encoded in the gradient of the regular part of a surface Green's function for a second order linear operator of the form $\Delta_g + \mathbf{v}(x, y) \cdot \nabla + V(x, y)$, for some velocity vector $\mathbf{v}(x, y)$ and effective potential $V(x, y)$, where Δ_g is the Laplace-Beltrami operator corresponding to metric tensor $g(x, y)$. We compute this quantity using the analytic-numerical framework that we first introduced in [Nonlinearity, **33**, pp. 643-674], and demonstrate that it is critical for the accurate prediction of spot motion. All numerical results are confirmed by finite element solutions of the full PDE system.

Keywords: singularly perturbed reaction-advection-diffusion system, localized vegetation patterns, surface Green's function, matched asymptotic analysis, Hadamard parametrix, microlocal analysis

1. Introduction

Reaction-diffusion systems of activator-inhibitor types have long been used to study pattern formation in various biological, chemical, and ecological systems (see e.g., [35, 43]). With sufficiently small activator-inhibitor diffusivity ratio, Turing showed that spatially homogeneous steady-state solutions can become unstable to spatial perturbations when a bifurcation parameter is varied [51]. Near onset, the system can support small-amplitude periodic spatial patterns characterized by a certain wavelength predicted by linear stability analysis. A weakly nonlinear analysis, based on that developed for the one-component system in [36], can be used to derive amplitude equations that describe slow time and long spatial scale evolution of the small-amplitude patterns and identify secondary instabilities. This theory, however, has limited application well above onset where patterns may exhibit large amplitudes with high degrees of spatial localization and complex dynamics. Such patterns were first computed numerically by Pearson in the two-dimensional Gray-Scott model [41], and observed experimentally in a chemical reaction by Lee et al. [33]. See [56] for a brief survey of asymptotic methods for analyzing small- and large-amplitude patterns.

Since the computations of [41], many works have sought to analytically describe the existence, stability, and dynamics of such patterns [56]. The specific regime where the activator-inhibitor diffusivity ratio is asymptotically small ($\mathcal{O}(\varepsilon^2) \ll 1$) has received particularly strong interest due to its amenability to analysis through matched asymptotic methods. In this singularly perturbed regime, solutions exist characterized by an activator component that is exponentially small everywhere in the domain except for

*Department of Mathematics and Statistics, Macquarie University, Sydney, NSW, Australia justin.tzou@mq.edu.au.
†School of Mathematics and Statistics, University of Sydney, Sydney, NSW, Australia leo.tzou@gmail.com.
Funding: The second author was supported by grants ARC DP190103451 and ARC DP190103302.

localized regions of extent $\mathcal{O}(\varepsilon)$ in which it is large. Interaction between spots is mediated through the inhibitor component, which varies on an $\mathcal{O}(1)$ spatial scale. The presence of large amplitudes far from the uniform equilibrium, along with large gradients in the activator component, necessitate the use of analytic techniques beyond those of the traditional linear and weakly nonlinear analyses used to treat small amplitude patterns near the Turing threshold.

In one-dimension, the geometric singular perturbation theory approach of Doelman et al. [13, 16, 15, 12] and the matched asymptotics/Green's function approach of Ward et al. [21, 58, 27] were successfully employed to obtain explicit results for the existence, stability and dynamics of localized spike solutions in reaction diffusion systems such as the Schnakenberg, Gray-Scott, and Gierer-Meinhardt models. For the two-dimensional Schnakenberg model on the unit disk, the hybrid asymptotic-numerical method of Ward et al. [57] was used to derive a threshold for the spot self-replication instability, along with a system of differential-algebraic equations describing the slow drift of spots. Using an adaptation of the same techniques, the analogous problem inside the three-dimensional unit sphere was solved for the Schnakenberg model [53].

While there have been many numerical studies of pattern formation on curved surfaces (see, e.g., [31, 40, 2, 7]), analytic results are much more sparse. For large amplitude localized spot patterns, [44, 49] and [52] analyzed the stability and dynamics of spot patterns on the surface of the unit sphere and torus, respectively. In the latter case, a new analytic-numerical framework based on techniques from microlocal analysis was developed for the accurate computation of the regular part of Green's functions along with its gradient. This framework was combined with the hybrid asymptotic-numerical framework to describe curvature-driven spot dynamics due to non-constant surface curvature. While this framework was developed to compute Green's functions for a general second order linear operator with spatially dependent first order and potential terms on a general curved surface, [52] only considered a simple model with no advection and a constant potential. In this work, we utilize the framework in its full generality. To provide a physical context for scenarios in which this generality of framework is required, we will demonstrate our methods on a model for patterned vegetation on a curved terrain, which, as proposed in [18], naturally gives rise to spatially dependent advection and potential terms. We also demonstrate how to incorporate these effects into the asymptotic analysis within the setting of a curved surface. We note, however, that the methods we employ here may be applicable to analyses of localized spot patterns in other reaction-advection-diffusion models on curved surfaces pertaining to other ecological and/or biological systems. We refer the reader to [30, 29] and the references therein for a sampling of such applications.

Beginning with the introduction of the original Klausmeier model [22], many works have studied the formation of vegetation patterns in semi-arid environments in the context of pattern formation in reaction-diffusion systems (see e.g., [46, 47, 42, 19, 38, 9, 45] and references therein). Most models consider the simple case of the two-component system for soil water concentration and vegetation density. Different models have been proposed for the modeling of the groundwater component. The original Klausmeier model considered only flow of the water down a (flat) hill with an advection term, omitting diffusion effects. In [54], linear and nonlinear diffusion of the groundwater were considered, leading to the 'generalized Klausmeier-Gray-Scott model', reducing to the classic Gray-Scott model [16] in the absence of advection. In one-dimensional versions of such models, it is well-known that the effect of the constant slope is to cause an uphill drift of the (one-dimensional) vegetation stripe patterns [6, 47]. In the two-dimensional extension, it has recently been shown [48, 25, 3] that a sufficiently steep slope can stabilize a stripe pattern and prevent a transition into a spotted pattern via a zigzag or breakup instability [23].

More detailed models have sought to account for the varying topography of the terrain on which the vegetation patterns form (see [18] for an overview of different models). In [18], terrain curvature was modeled using a non-constant advection term in the groundwater dynamics, along with a linear term accounting for dispersion of water from ridges and accumulation in valleys. It was shown numerically that the inclusion of the latter term produced the arcing of vegetation stripes observed in nature [34]. In [1], a detailed numerical study of the effect of terrain topography on the dynamics and distribution of vegetation stripes was performed.

Instabilities due to decreasing resources [20, 42] or landscape features [25] can cause vegetation stripe patterns to break up into localized spot patterns. These spot patterns can subsequently undergo further instabilities and dynamics, such as self-replication, annihilation, and drift [5]. While hybrid asymptotic-numerical methods for spot patterns in reaction-diffusion systems have been developed for flat domains [28] along with spherical [49, 44] and toroidal [52] surfaces, such analyses have not been performed with general advection terms on general surfaces. Motivated by numerical studies of the effect of curvature on vegetation patterns [18, 1], we seek to develop a framework to tackle the problem from a hybrid analytic-numerical perspective.

Our goal here is to provide this new framework in the context of spotted vegetation patterns in a system of reaction-advection-diffusion equations with spatially-dependent advection and potential terms. We seek to analytically describe ways in which spot motion is impacted by the topography of the surface on which it forms. While we perform the analysis in the context of a specific model for vegetation patterns, we emphasize that our method is applicable to a *general* curved surface and to *general* advection and potential terms. For example, [29] studies the influence of advection on pattern formation on the surface of the sphere, while [30, 55, 2] considers the dynamics of patterns on an evolving surface. We remark that the latter scenario of growing domains (in the asymptotic limit of slow growth) gives rise to advection and linear growth and decay terms similar in form to those in the model that we consider below.

We now introduce a coordinate-invariant reaction-advection-diffusion system for vegetation density and soil water on a terrain with elevation given by $Z = \tilde{\zeta}(X, Y)$. The system involves only operators and quantities that account for the intrinsic geometry of the surface on which it is posed, allowing it to be written in a coordinate-free formulation.

1.1. **A coordinate-invariant model.** Inspired by [18] (cf. Table 1.1, along with Eqs. (1.1)-(1.2)), which studies effects of topography on banded vegetation patterns, the model that we propose accounts for the heterogeneous rates of water flow and dispersal due to the slope and curvature of the terrain. Our modified system involves quantities intrinsic to the surface on which the system is posed, as well as the natural definitions of operators with respect to the corresponding curved metric. Thus, for vegetation density V and soil water concentration U on a terrain with elevation described by $\tilde{Z} = \tilde{\zeta}(X, Y)$, we propose the coupled system of equations

$$V_t = \tilde{D}_V \Delta_{\tilde{g}} V - \tilde{m} V + UV^2\,, \qquad t > 0\,, \quad (X, Y) \in [0, L_X] \times [0, L_Y]\,, \tag{1.1a}$$

$$U_t = \tilde{D}_U \Delta_{\tilde{g}} U + \mathrm{div}_{\tilde{g}}(\tilde{\mathbf{c}} U) + \frac{a}{\sqrt{|\tilde{g}|}} - \tilde{p}\sqrt{|\tilde{g}|} U - UV^2\,, \qquad t > 0\,, \quad (X, Y) \in [0, L_X] \times [0, L_Y]\,, \tag{1.1b}$$

where $\tilde{m}$, $\tilde{D}$, and $\tilde{p}$ are constants. We make a few remarks regarding the form of and terms in (1.1). We have included a second order term $\tilde{D}\Delta_{\tilde{g}} U$ to account for the diffusion of soil water, where $\Delta_{\tilde{g}}$ is the Laplace-Beltrami operator with respect to the metric tensor $\tilde{g}$ specified by the graph $\tilde{Z} = \tilde{\zeta}(X, Y)$. The transport term, $\tilde{c}\,\mathrm{div}_{\tilde{g}}(\tilde{\mathbf{c}} U)$, with constant $\tilde{c}$ and vector $\tilde{\mathbf{c}}$ specified and discussed below and in Appendix A, models transport of water in the direction opposite to the gradient of $\tilde{\zeta}$. Importantly, $\tilde{\mathbf{c}}$ will account only for the component of the velocity of transport in the X-Y plane and is given by

$$\tilde{\mathbf{c}} = \tilde{c}(1 + \tilde{\zeta}_X^2 + \tilde{\zeta}_Y^2)^{-1}(\tilde{\zeta}_X, \tilde{\zeta}_Y)\,, \tag{1.1c}$$

in the coordinate given by $(X, Y) \mapsto (X, Y, \tilde{\zeta}(X, Y))$; herein, we consider the surface from an intrinsic perspective rather than as an object embedded in $\mathbb{R}^3$. The scaling by the surface element $\sqrt{|\tilde{g}|}$ for the rainfall term $a/\sqrt{|\tilde{g}|}$ models vertical rainfall on a curved surface; indeed, the total amount of rainfall over a fixed region in the X-Y plane must be independent of the features of the surface within that region. Similarly, the rate of evaporation must be proportional to the exposed surface area; hence the prefactor $\sqrt{|\tilde{g}|}$ on the decay term in (1.1b). Here, $|\tilde{g}|$ denotes the determinant of the metric tensor $\tilde{g}$.

Under a rescaling of (1.1) (see Appendix A), on the surface $z = \zeta(\theta_1, \theta_2)$ we obtain the coupled system

$$v_t = \varepsilon^2 \Delta_g v - v + Auv^2\,, \qquad t > 0\,, \quad (\theta_1, \theta_2) \in [0, 2\pi] \times [0, L_{\theta_2}]\,, \tag{1.2a}$$

$$\tau u_t = D\Delta_g u - \mathbf{c}(\boldsymbol{\theta}) \cdot \nabla u + \frac{1}{\sqrt{|g(\boldsymbol{\theta})|}} - \mathcal{V}(\boldsymbol{\theta})u - uv^2\,, \qquad t > 0\,, \quad (\theta_1, \theta_2) \in [0, 2\pi] \times [0, L_{\theta_2}]\,, \tag{1.2b}$$

$$\mathbf{c}(\boldsymbol{\theta}) \equiv -c\frac{1}{|g(\boldsymbol{\theta})|}\nabla\zeta\,, \quad \mathcal{V}(\boldsymbol{\theta}) \equiv \sqrt{|g(\boldsymbol{\theta})|} - c\frac{2}{\sqrt{|g(\boldsymbol{\theta})|}}H(\boldsymbol{\theta})\,, \quad \zeta = \zeta(\boldsymbol{\theta})\,; \quad \boldsymbol{\theta} \equiv \begin{pmatrix} \theta_1 \\ \theta_2 \end{pmatrix}\,, \tag{1.2c}$$

with positive $\mathcal{O}(1)$ constants c and D, while for the spot regime, we require $A \sim \mathcal{O}(\varepsilon|\log\varepsilon|)$ (see [8]). For (1.2), we impose periodic conditions in θ_1 and θ_2. As such, we study a patch of the terrain that is assumed to be periodically extended; i.e., $\zeta(\theta_1, \theta_2)$ is 2π-periodic in θ_1 and L_{θ_2}-periodic in θ_2. In (1.2b) and(1.2c), the gradient ∇ and dot product $\cdot$ operators are both defined with respect to the flat (identity) metric, $\sqrt{|g(\boldsymbol{\theta})|}$ is the surface element of the graph $\zeta(\boldsymbol{\theta})$, while $H(\boldsymbol{\theta})$ denotes the mean curvature of the surface $\mathcal{M}$ at the point $\boldsymbol{\theta}$, and is given by

$$H(\boldsymbol{\theta}) = \frac{1}{2\sqrt{|g|}}g^{ij}\zeta_{\theta_i\theta_j}\,; \qquad |g| = 1 + \zeta_{\theta_1}^2 + \zeta_{\theta_2}^2\,, \tag{1.2d}$$

where we have used the Einstein summation notation. The components g_{ij} of the metric tensor g are given below in terms of $\zeta(\boldsymbol{\theta})$ and its partial derivatives. In (1.2d), g^{ij} denotes the i-j-th component of the inverse of the metric tensor g, while f_{θ_i} denotes the partial derivative of $f(\boldsymbol{\theta})$ with respect to θ_j. With this scaling, (1.2) reduces to the rescaled Gray-Scott model considered in [8] when the surface is flat (e.g., $\zeta \equiv 0$).

We make several remarks regarding (1.2), which will be the form of the model that we consider in §2 - §4. First, we note that the divergence term in (1.1b) integrates to zero over the periodic domain. In (1.2b) and (1.2c), we have written the divergence term as the sum of a transport term $\mathbf{c} \cdot \nabla u$ along with a growth/decay term $2c|g|^{-1/2}H(\boldsymbol{\theta})u$. The latter term may be interpreted (see [18]) as the accumulation of water on "valley lines" and the diversion of water away from "ridge lines," and together with the evaporation term $\sqrt{|g(\boldsymbol{\theta})|}$, make up the spatially variable potential $-\mathcal{V}(\boldsymbol{\theta})$. The former term models the transport of water in the direction of steepest decrease of ζ. Compared to [18], it contains two extra factors of $|g|^{-1/2}$; in Appendix A, we discuss this origin of this term from both a physical and mathematical perspective. We also emphasize that the $1/\sqrt{|g|}$ term does not correspond to spatially-dependent precipitation, but rather to the uniform vertical rainfall reaching the surface at non-uniform concentrations due to the latter's curved topography.

For completeness, we now express the PDE system of (1.1) in a geometric and coordinate-free form, which will demonstrate that (1.1) is coordinate-invariant. We remark that coordinate-invariance may apply to any hypersurface $\mathcal{S}$, which need not be periodic as the surface $\mathcal{M}$ that we consider here. Furthermore, all of the analytic and numerical methods that we employ in §2 are valid for any boundary condition on $\mathcal{S}$. In Appendix A, we discuss in detail the equivalence between (1.1) and (1.3).

Endow $\mathbb{R}^3$ with the usual Euclidean metric $\langle\cdot,\cdot\rangle_{\mathrm{e}}$ and let E be a parallel (i.e. constant) unit vector field with respect to the Levi-Civita connection. This vector field represents gravity. Let $\mathcal{M}$ be a hyper-surface which is transversal to E. The system (1.1) can be written as

$$V_t = \Delta_{\tilde{g}}V - \tilde{m}V + UV^2\,, \tag{1.3a}$$

$$U_t = \tilde{D}\Delta_{\tilde{g}}U + \mathrm{div}_{\tilde{g}}(\tilde{\mathbf{c}}U) + a|\langle E, \tilde{\nu}\rangle_{\mathrm{e}}| - \tilde{p}|\langle E, \tilde{\nu}\rangle_{\mathrm{e}}|^{-1}U - UV^2\,, \tag{1.3b}$$

where $\tilde{\mathbf{c}} \in T\mathcal{M}$ is the unique vector satisfying $D\iota_{\mathcal{M}}\tilde{\mathbf{c}} = E - \langle E, \tilde{\nu}\rangle_{\mathrm{e}}\tilde{\nu}$, the projection of E onto $T\mathcal{M} \subset T\mathbb{R}^3$. That is, $\tilde{\mathbf{c}}$ is the tangential component of E to $\mathcal{M}$ with respect to the Euclidean metric. Here, $\tilde{\nu}$ is the unit normal vector to $\mathcal{M}$ in the E direction, and $\iota_{\mathcal{M}} : \mathcal{M} \hookrightarrow \mathbb{R}^3$ denotes the inclusion map, and $D\iota_{\mathcal{M}}$ is the differential map/pushforward mapping $T\mathcal{M}$ to $T\mathbb{R}^3$.

Finally, we remark on the coordinate invariance of (1.2). We observe that $\mathrm{div}_g(\mathbf{c}u) = u\mathrm{div}_g\mathbf{c} + du(\mathbf{c})$. Since $\mathbf{c} = E - \langle\tilde{\nu}, E\rangle_{\mathrm{e}}\tilde{\nu}$, we have that $\mathrm{div}_g(\mathbf{c}u) = u\mathrm{div}_g(\mathbf{c}) + du(E)$ owing to the fact that $\tilde{\nu}$ vanishes on $T^*\mathcal{M}$ by definition, where $T^*\mathcal{M}$ is the cotangent bundle of $\mathcal{M}$. The quantity $\mathrm{div}_g\mathbf{c}$ can be calculated by using the fact that in the coordinate system given by $(X, Y, \zeta(X, Y))$, $\mathbf{c}$ is given by (1.2c). We compute

$$\mathrm{div}_g\mathbf{c} = -c\frac{\zeta_{\theta_1\theta_1}(1+\zeta_{\theta_2}^2) + \zeta_{\theta_2\theta_2}(1+\zeta_{\theta_1}^2) - 2\zeta_{\theta_1}\zeta_{\theta_2}\zeta_{\theta_1\theta_2}}{(1+\zeta_{\theta_1}^2+\zeta_{\theta_2}^2)^2} = -2c|\langle\nu, E\rangle_{\mathrm{e}}|H\,,$$

where H is the mean curvature given in (1.2d). This leads to the following coordinate-free formulation of (1.2)

$$v_t = \varepsilon^2\Delta_g v - v + Auv^2\,, \qquad t > 0\,, \tag{1.4a}$$

$$\tau u_t = D\Delta_g u + cdu(E) + |\langle\nu, E\rangle_{\mathrm{e}}| + \left(2c|\langle\nu, E\rangle_{\mathrm{e}}|H - |\langle\nu, E\rangle_{\mathrm{e}}|^{-1}\right)u - uv^2\,, \qquad t > 0\,, \tag{1.4b}$$

demonstrating that (1.2) is indeed coordinate-invariant. We emphasize that we make no claim that our model is in any way more accurate than that introduced in [18], on which our model is based. We only submit that when considering diffusive and advective transport on a curved surface $\mathcal{M}$, our model in (1.2), and its coordinate-free formulation (1.4), takes account only of the intrinsic geometry of $\mathcal{M}$ (modulo the direction transverse to the surface required for rainfall), which may make it a more natural formulation from a geometric perspective. Our primary purpose here, however, remains to demonstrate a method for analyzing localized spot solutions to a singularly perturbed reaction-advection-diffusion system on a curved surface.

In the $0 < \varepsilon^2 \ll 1$ limit of slow activator diffusivity, we use the hybrid asymptotic-numerical method pioneered by Ward et al. (see e.g, [57, 28, 24]) to construct a quasi-equilibrium localized one-spot solution to (1.2) on a curved surface $\mathcal{M}$. Furthermore, we analyze the impact of the surface curvature and slope on the drift dynamics of the spots; in particular, we show that the advection due to the *slope* of the surface $\mathcal{M}$ along with the spatially variable potential and source term both have an $\mathcal{O}(\varepsilon^2|\log\varepsilon|)$ effect on motion, while the *curvature* of $\mathcal{M}$ has an $\mathcal{O}(\varepsilon^2)$ effect. These effects differ by a $|\log\varepsilon|$ factor and are thus comparable when ε is only moderately small; we show that accurate computation of all terms is required to predict spot motion.

The outline of the paper is as follows. In §2, begin with geometric preliminaries before constructing a one-spot quasi-equilibrium solution to (1.2). We then we derive a system of differential-algebraic equations (DAE) that couples the slow motion of the spot with its amplitude as it moves over the surface of varying potential and source. In contrast to previous works on spot dynamics, our analysis accounts for a general advection, potential terms, and source terms in the global variable. We find that the motion is a function of three effects: surface curvature, advection, and the spatially varying potential and source term. While the latter two effects are larger by a factor of $|\log\varepsilon| \gg 1$, we show that all three effects must be accounted for in order to accurately predict spot motion. To do so, we will require an accurate computation of the gradient of the regular part R of a certain Green's function, defined in (2.3b). To simplify analysis, we will compute this quantity in the normal coordinates centered about the center of the spot. In §3, we will isolate these effects to understand how they each affect spot motion, and compare the asymptotic predictions of spot motion to full numerical solutions of the PDE system (1.2b). In §4, we demonstrate the dynamic triggering of the spot splitting instability (see [8] and [28]) due to slow drift of the spot, and numerically demonstrate the transition from spots patterns to stripe-like structures as the feed-rate is slowly increased. In §5, we summarize our findings and discuss some open problems.

2. Quasi-equilibrium solution and spot dynamics

2.1. **Geometric preliminaries.** To construct a quasi-equilibrium one-spot solution and determine its slow dynamics, we will require the accurate computation of a certain Green's function. To this end, we will apply the analytic-numerical method first developed in [52] for the purpose of analyzing spot patterns on the surface of a ring torus. In [52], the method was used to compute properties of the regular part of two Green's functions: the source-neutral Green's function G_N satisfying

$$\Delta_g G_N = \frac{1}{|\Omega|} - \delta(\boldsymbol{\theta};\boldsymbol{\theta}_0)\,; \qquad \int_\Omega G_N\, d\boldsymbol{\theta} = 0\,, \tag{2.1a}$$

$$G_N(\boldsymbol{\theta};\boldsymbol{\theta}_0) \sim -\frac{1}{2\pi}\log d_g(\boldsymbol{\theta},\boldsymbol{\theta}_0) + R_N(\boldsymbol{\theta};\boldsymbol{\theta}_0) \ \text{ as } \ \boldsymbol{\theta}\to\boldsymbol{\theta}_0\,, \tag{2.1b}$$

and the Helmholtz Green's function G_H satisfying

$$\Delta_g G_H - kG_H = -\delta(\boldsymbol{\theta};\boldsymbol{\theta}_0)\,, \tag{2.2a}$$

$$G_H(\boldsymbol{\theta};\boldsymbol{\theta}_0) \sim -\frac{1}{2\pi}\log d_g(\boldsymbol{\theta},\boldsymbol{\theta}_0) + R_H(\boldsymbol{\theta};\boldsymbol{\theta}_0) \ \text{ as } \ \boldsymbol{\theta}\to\boldsymbol{\theta}_0\,, \tag{2.2b}$$

for some constant k and periodic conditions in $\boldsymbol{\theta}$. In (2.1) and (2.2), as well as below, we denote as $d_g(\boldsymbol{\theta},\boldsymbol{\theta}_0)$ the geodesic distance between $\boldsymbol{\theta}$ and $\boldsymbol{\theta}_0$ with respect to the metric tensor g. We also recall the definition of $\boldsymbol{\theta} = (\theta_1,\theta_2)^T \in \Omega$ in (1.2c) as the vector of the two variables parametrizing the surface. In order to analyze the more general reaction-advection-diffusion system of (1.2), however, we must consider the more involved case of the Green's function G satisfying

$$-\Delta_g G + \frac{1}{D}\mathbf{c}(\boldsymbol{\theta})\cdot\nabla G + \frac{1}{D}\mathcal{V}(\boldsymbol{\theta})G = \delta(\boldsymbol{\theta};\boldsymbol{\theta}_0)\,, \tag{2.3a}$$

$$G(\boldsymbol{\theta};\boldsymbol{\theta}_0) \sim -\frac{1}{2\pi}\log d_g(\boldsymbol{\theta},\boldsymbol{\theta}_0) + \boldsymbol{\gamma}\cdot(\boldsymbol{\theta}-\boldsymbol{\theta}_0)\log d_g(\boldsymbol{\theta},\boldsymbol{\theta}_0) + R(\boldsymbol{\theta}_0;\boldsymbol{\theta}_0) + (\boldsymbol{\theta}-\boldsymbol{\theta}_0)\cdot\nabla\, R(\boldsymbol{\theta};\boldsymbol{\theta}_0)|_{\boldsymbol{\theta}_0}\ , \ \text{ as } \ \boldsymbol{\theta}\to\boldsymbol{\theta}_0\,, \tag{2.3b}$$

with periodicity conditions in θ_1 and θ_2. The dot product involving the $\boldsymbol{\gamma}$ term in (2.3b), which appears due to the presence of the advection term of (2.3a), is with respect to the flat metric. In [59], an expression for $\boldsymbol{\gamma}$ was derived for the special case of rotational advection in the unit disk. Here, we show in this more general case that the term arises naturally via the construction of a parametrix near $\boldsymbol{\theta}_0$. From a computational perspective, its presence increases the difficulty of numerically isolating the regular part $R(\boldsymbol{\theta};\boldsymbol{\theta}_0)$ and subsequently computing $\nabla R(\boldsymbol{\theta};\boldsymbol{\theta}_0)|_{\boldsymbol{\theta}=\boldsymbol{\theta}_0}$, the value of the gradient of R at $\boldsymbol{\theta}_0$.

The computation of $\nabla R(\boldsymbol{\theta};\boldsymbol{\theta}_0)|_{\boldsymbol{\theta}=\boldsymbol{\theta}_0}$, along with the asymptotic analysis of slow spot dynamics in §2.2, will be performed in Riemannian normal coordinates, which are obtained via an exponential map defined below. We define here some quantities required to compute map; for more details, see [32, 11]. The metric tensor $g_{ij}(\boldsymbol{\theta})$ is specified by the graph $z = \zeta(\boldsymbol{\theta})$. That is, let $J(\boldsymbol{\theta})$ be the Jacobian matrix given by

$$J(\boldsymbol{\theta}) = \begin{pmatrix} 1 & 0 \\ 0 & 1 \\ \zeta_{\theta_1} & \zeta_{\theta_2} \end{pmatrix}.$$

The (positive-definite) metric tensor $(g_{ij}(\boldsymbol{\theta}))$ is then given by $(g_{ij}(\boldsymbol{\theta})) = J^T J$ as

$$(g_{ij}) = \begin{pmatrix} \tilde{E} & \tilde{F} \\ \tilde{F} & \tilde{G} \end{pmatrix}, \qquad \tilde{E} \equiv 1+\zeta_{\theta_1}^2\,, \quad \tilde{F} \equiv \zeta_{\theta_1}\zeta_{\theta_2}\,, \quad \tilde{G} \equiv 1+\zeta_{\theta_2}^2\,; \quad |g| = 1+\zeta_{\theta_1}^2+\zeta_{\theta_2}^2\,, \tag{2.4}$$

where $\cdot^T$ denotes the transpose. The eigenvalues λ_1 and λ_2 and corresponding normalized eigenvectors $\mathbf{v}_1$ and $\mathbf{v}_2$ of the matrix g in (2.4) are given by

$$\lambda_1 = 1+\zeta_{\theta_1}^2+\zeta_{\theta_2}^2\,, \quad \mathbf{v}_1 = \frac{1}{\sqrt{\zeta_{\theta_1}^2+\zeta_{\theta_2}^2}}\begin{pmatrix}\zeta_{\theta_1}\\ \zeta_{\theta_2}\end{pmatrix}; \qquad \lambda_2 = 1\,, \quad \mathbf{v}_2 = \frac{1}{\sqrt{\zeta_{\theta_1}^2+\zeta_{\theta_2}^2}}\begin{pmatrix}-\zeta_{\theta_2}\\ \zeta_{\theta_1}\end{pmatrix}. \tag{2.5}$$

With (g_{ij}) in (2.5) symmetric, we define the orthogonal matrix P and diagonal matrix Λ

$$P(\boldsymbol{\theta}) = (\mathbf{v}_1\ \ \mathbf{v}_2)\,, \qquad \Lambda(\boldsymbol{\theta}) = \begin{pmatrix}\lambda_1 & 0\\ 0 & \lambda_2\end{pmatrix}, \tag{2.6}$$

so that $(g_{ij}) = P\Lambda P^T$. We thus have that, for some $\mathbf{x}\in\mathbb{R}^2$, $\mathbf{x}^T(g_{ij})\mathbf{x} = \mathbf{x}^T(P\Lambda^{1/2})(P\Lambda^{1/2})^T\mathbf{x}$. That is, under the transformation $\mathbf{x} = P\Lambda^{-1/2}\mathbf{w}$, the metric tensor (g_{ij}) transforms to the identity matrix at $\boldsymbol{\theta}$.

The Christoffel symbols, which we require for an exponential map to be discussed below, are given in terms of $\tilde{E}$, $\tilde{F}$, and $\tilde{G}$ by

$$\begin{aligned}
&\alpha\Gamma_{11}^1 = \tilde{G}\tilde{E}_{\theta_1} - 2\tilde{F}\tilde{F}_{\theta_1} + \tilde{F}\tilde{E}_{\theta_2}\,, && \alpha\Gamma_{12}^1 = \tilde{G}\tilde{E}_{\theta_2} - \tilde{F}\tilde{G}_{\theta_1}\,, && \alpha\Gamma_{22}^1 = 2\tilde{G}\tilde{F}_{\theta_2} - \tilde{G}\tilde{G}_{\theta_1} - \tilde{F}\tilde{G}_{\theta_2}\\
&\alpha\Gamma_{11}^2 = 2\tilde{E}\tilde{F}_{\theta_1} - \tilde{E}\tilde{E}_{\theta_2} - \tilde{F}\tilde{E}_{\theta_1}\,, && \alpha\Gamma_{12}^2 = \tilde{E}\tilde{G}_{\theta_1} - \tilde{F}\tilde{E}_{\theta_2}\,, && \alpha\Gamma_{22}^2 = \tilde{E}\tilde{G}_{\theta_2} - 2\tilde{F}\tilde{F}_{\theta_2} + \tilde{F}\tilde{G}_{\theta_1}\,,
\end{aligned} \tag{2.7}$$

where $\alpha \equiv 2(\tilde{E}\tilde{G}-\tilde{F}^2)$ and $\Gamma_{12}^k = \Gamma_{21}^k$. Also needed for the exponential map is the second fundamental form for the surface $z=\zeta(\boldsymbol{\theta})$, the matrix for which is given by

$$II_p = \begin{pmatrix}\tilde{L} & \tilde{M}\\ \tilde{M} & \tilde{N}\end{pmatrix}, \qquad \tilde{L} = \frac{\zeta_{\theta_1\theta_1}}{\sqrt{|g|}}\,, \quad \tilde{M} = \frac{\zeta_{\theta_1\theta_2}}{\sqrt{|g|}}\,, \quad \tilde{N} = \frac{\zeta_{\theta_2\theta_2}}{\sqrt{|g|}}\,. \tag{2.8}$$

The gradient and Laplace-Beltrami operators with respect to the metric g are

$$(\nabla_g)^i \equiv g^{ij}\partial_{\theta_j}\,, \qquad \Delta_g \equiv \frac{1}{\sqrt{|g|}}\partial_{\theta_i}\left(\sqrt{|g|}g^{ij}\partial_{\theta_j}\right), \tag{2.9}$$

where g^{ij} is the i-jth component of the inverse of the matrix $g(\boldsymbol{\theta})$, and is given by

$$\left(g^{ij}\right) = \frac{1}{|g|}\begin{pmatrix}\tilde{G} & -\tilde{F}\\ -\tilde{F} & \tilde{E}\end{pmatrix}. \tag{2.10}$$

Lastly, the surface element on $z=\zeta(\boldsymbol{\theta})$ is given by $\sqrt{|g|}$, and so the delta source on the right-hand side of (2.3) is given explicitly by

$$\delta(\boldsymbol{\theta};\boldsymbol{\theta}_0) = \frac{1}{\sqrt{|g|}}\delta(\theta_1-\theta_1^0)\delta(\theta_2-\theta_2^0)\,, \qquad \boldsymbol{\theta}_0 \equiv \begin{pmatrix}\theta_1^0\\ \theta_2^0\end{pmatrix}, \tag{2.11}$$

where $\delta(\theta_j-\theta_j^0)$ is the one-dimensional Dirac delta function centered at θ_j^0.

The matched asymptotic analysis, whereby the inner solutions near the $\mathcal{O}(\varepsilon)$ region of the spot are matched to a global outer solution, will proceed as in [49, 44] for the surface of the unit sphere and [52] for the surface of the ring torus. In these works, the inner coordinates near the point $\mathbf{r}\in\mathbb{R}^3$ on the surface were of the form $\mathbf{r}(\boldsymbol{\theta}) = \mathbf{r}(\boldsymbol{\theta}_0) + \varepsilon P(\boldsymbol{\theta}_0)\mathbf{s}$, where $\mathbf{r}$ specifies the embedding of the surface in $\mathbb{R}^3$, and $\mathbf{s}\in\mathbb{R}^2$. The matrix $P(\boldsymbol{\theta}_0)$ is a 3×2 matrix chosen so that, in the local tangent plane coordinates $\mathbf{s}=(s_1,s_2)$ centered at $\boldsymbol{\theta}_0$, the Laplace-Beltrami operator Δ_g of (2.9) takes the form

$$\Delta_g \sim \frac{1}{\varepsilon^2}\left(\partial_{s_1}^2 + \partial_{s_2}^2\right) + \mathcal{O}(\varepsilon^{-1})\,. \tag{2.12}$$

The $\mathcal{O}(\varepsilon^{-1})$ correction term in (2.12) for the surface curvature at $\mathbf{r}(\boldsymbol{\theta}_0)$ gives rise to a nonhomogeneous term in the expansion for which an additional analysis is required in order to resolve the spot dynamics.

In this paper, we will instead exploit the properties of Riemannian normal coordinates near $\boldsymbol{\theta}_0$ in order to obtain an asymptotic for Δ_g for which the correction term is $\mathcal{O}(1)$ instead of $\mathcal{O}(\varepsilon^{-1})$ (see Appendix A of [50]). That is, let $\mathbf{x} \equiv (x^1, x^2)^T \in \mathbb{R}^2$. Then the exponential map is given by $\boldsymbol{\theta}_{\boldsymbol{\theta}_0}(\mathbf{x}) = \tilde{\boldsymbol{\gamma}}_{P\Lambda^{-1/2}\mathbf{x}}(1)$, where $\tilde{\boldsymbol{\gamma}}_{P\Lambda^{-1/2}\mathbf{x}}$ is the unique geodesic satisfying the initial conditions $\tilde{\boldsymbol{\gamma}}_{P\Lambda^{-1/2}\mathbf{x}}(0) = \boldsymbol{\theta}_0$ and $\dot{\tilde{\boldsymbol{\gamma}}}_{P\Lambda^{-1/2}\mathbf{x}}(0) = P\Lambda^{-1/2}\mathbf{x}$. Here, $P = P(\boldsymbol{\theta}_0)$ and $\Lambda = \Lambda(\boldsymbol{\theta}_0)$ are matrices defined in (2.6). For $\tilde{\boldsymbol{\gamma}}_{P\Lambda^{-1/2}\mathbf{x}}(t) \equiv (\tilde{\gamma}^1(t), \tilde{\gamma}^2(t))$, the geodesic equation is given by

$$\dot{\tilde{\gamma}}^k(t) = \xi^k(t)\,, \qquad \dot{\xi}^k(t) = -\xi^i(t)\xi^j(t)\Gamma_{ij}^k(\tilde{\boldsymbol{\gamma}}_{P\Lambda^{-1/2}\mathbf{x}}(t))\,; \qquad k = 1, 2\,, \tag{2.13a}$$

$$(\tilde{\gamma}^1(0), \tilde{\gamma}^2(0)) = \boldsymbol{\theta}_0\,, \qquad (\xi^1(0), \xi^2(0)) = P(\boldsymbol{\theta}_0)\Lambda^{-1/2}(\boldsymbol{\theta}_0)\mathbf{x}\,, \tag{2.13b}$$

$$\boldsymbol{\theta}(\mathbf{x}) = \tilde{\boldsymbol{\gamma}}_{P\Lambda^{-1/2}\mathbf{x}}(1)\,, \tag{2.13c}$$

where the Christoffel symbols Γ_{ij}^k are given in (2.7). In (2.13), $\mathbf{x}$ are the Riemannian normal coordinates, while $\boldsymbol{\theta}$ are the original coordinates parametrizing the surface.The lower bound for the radius of injectivity on $\mathcal{M}$, denoted $\mathrm{inj}(\mathcal{M})$, is given in terms of σ, the largest eigenvalue of the matrix II_p of (2.8), by

$$\mathrm{inj}(\mathcal{M}) = \frac{\pi}{\sigma}\,. \tag{2.14}$$

Under the transformation (2.13c), the Laplace-Beltrami operator Δ_g in $\boldsymbol{\theta}$ coordinates with metric tensor g transforms to $\Delta_{\hat{g}}$ in $\mathbf{x}$-coordinates. The metric tensor $\hat{g}(\mathbf{x})$ is given by

$$\hat{g}(\mathbf{x}) = \left(\frac{D\boldsymbol{\theta}}{D\mathbf{x}}\right)^T g(\boldsymbol{\theta}(\mathbf{x}))\frac{D\boldsymbol{\theta}}{D\mathbf{x}}\,; \qquad \frac{D\boldsymbol{\theta}}{D\mathbf{x}} \equiv \begin{pmatrix} \partial_{x^1}\boldsymbol{\theta} & \partial_{x^2}\boldsymbol{\theta} \end{pmatrix}. \tag{2.15}$$

As shown in [52], the metric tensor $\hat{g}(\mathbf{x})$ satisfies the property $\hat{g}(\mathbf{x}) = \hat{g}(\mathbf{0}) + \mathcal{O}(|\mathbf{x}|^2)$. With $\boldsymbol{\theta}(\mathbf{0}) = \boldsymbol{\theta}_0$ and $(D\boldsymbol{\theta}/D\mathbf{x})|_{\mathbf{x}=\mathbf{0}} = P(\boldsymbol{\theta}_0)\Lambda^{-1/2}(\boldsymbol{\theta}_0)$, we have that $\hat{g}(\mathbf{0}) = I_2$, where I_2 is the 2×2 identity matrix. With $\boldsymbol{\theta}(\mathbf{x}) = \gamma_{P\Lambda^{-1/2}\mathbf{x}}(1)$, the Laplace-Beltrami operator Δ_g in $\boldsymbol{\theta}$ coordinates transforms to $\Delta_{\hat{g}}$, which to leading order near $\mathbf{x} = \mathbf{0}$ is the Laplace operator on the flat metric. That is,

$$\Delta_{\hat{g}} \sim \Delta_{\mathbf{x}} + \mathcal{O}(|\mathbf{x}|)\partial_{x^i} + \mathcal{O}(|\mathbf{x}|^2)\partial_{x^i}^2\,, \tag{2.16}$$

where $\Delta_{\mathbf{x}}$ denotes the (flat) Laplacian in the $\mathbf{x}$ coordinates. The inner coordinates $\mathbf{y}$ describing the solution in the $\mathcal{O}(\varepsilon)$ region of the spot are then taken to be

$$\mathbf{y} \equiv \begin{pmatrix} y^1 \\ y^2 \end{pmatrix} = \frac{1}{\varepsilon}\mathbf{x}\,; \qquad \mathbf{x} \equiv \begin{pmatrix} x^1 \\ x^2 \end{pmatrix}. \tag{2.17}$$

We thereby obtain that the Laplace-Beltrami operator Δ_g in (2.9) has the expansion near $\boldsymbol{\theta}_0$ given by

$$\Delta_g \sim \frac{1}{\varepsilon^2}\Delta_{\mathbf{y}} \equiv \frac{1}{\varepsilon^2}\left(\partial_{y^1}^2 + \partial_{y^2}^2\right) + \mathcal{O}(1)\,, \tag{2.18}$$

as desired. In particular, the correction term of (2.18) is $\mathcal{O}(1)$ instead of $\mathcal{O}(\varepsilon^{-1})$ as in (2.12). In this way, for points near $\boldsymbol{\theta}_0$, we have the following relationships between $d_g(\boldsymbol{\theta}(\mathbf{x}), \boldsymbol{\theta}_0)$, $|\mathbf{x}|$, and $|\mathbf{y}|$:

$$d_g(\boldsymbol{\theta}(\mathbf{x}), \boldsymbol{\theta}_0) = |\mathbf{x}| = \varepsilon|\mathbf{y}|\,, \tag{2.19}$$

where $|\cdot|$ denotes the Euclidean norm, and $d_g(\boldsymbol{\theta}(\mathbf{x}), \boldsymbol{\theta}_0)$ the geodesic distance between $\boldsymbol{\theta}$ and $\boldsymbol{\theta}_0$. While most of the analysis will be performed in the normal coordinates, our results for spot motion will be given in terms of the original $\boldsymbol{\theta}$-coordinates.

We make a final remark that, while the framework that we present below can be applied to a general surface $z = \zeta(\boldsymbol{\theta})$, for concreteness, we will consider the surface

$$\zeta(\boldsymbol{\theta}) = k\cos(\theta_1)\cos(2\theta_2)\,; \qquad \theta_1 \in [0, 2\pi)\,, \quad \theta_2 \in [0, \pi)\,, \tag{2.20}$$

(i.e., $L_{\theta_1} = 2\pi$, $L_{\theta_2} = \pi$ in (1.2)) for some constant $k \geq 0$ that is $\mathcal{O}(1)$ with respect to ε; the analysis of §2.2 is valid for such surfaces whose curvature is independent of ε. Note that this surface satisfies periodicity conditions in both θ_1 and θ_2. For this surface, in Fig. 1, we plot the diagonal of the regular part $R(\boldsymbol{\theta}_0; \boldsymbol{\theta}_0)$, along with two components of its gradient, $\partial_{\theta_1} R(\boldsymbol{\theta}; \boldsymbol{\theta}_0)|_{\boldsymbol{\theta}=\boldsymbol{\theta}_0}$, and $\partial_{\theta_2} R(\boldsymbol{\theta}; \boldsymbol{\theta}_0)|_{\boldsymbol{\theta}=\boldsymbol{\theta}_0}$ on the surface given by (2.20). The colors correspond to the value of the quantity being plotted, not the height of the surface itself.

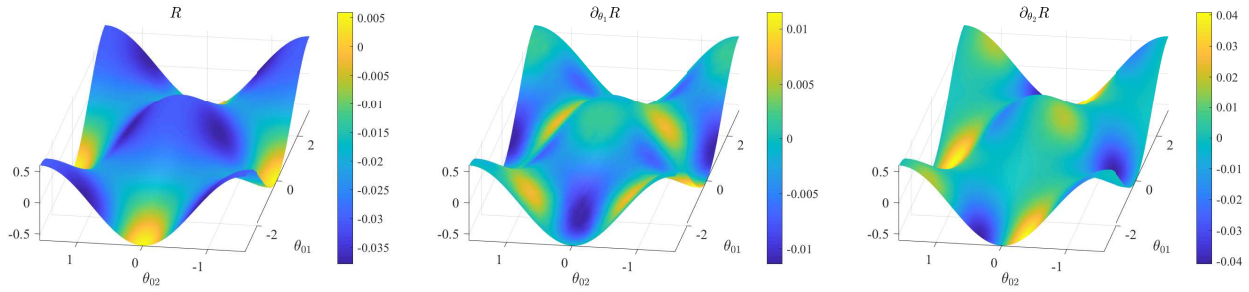

(a) $R(\boldsymbol{\theta}_0; \boldsymbol{\theta}_0)$ (b) $\partial_{\theta_1} R(\boldsymbol{\theta}; \boldsymbol{\theta}_0)|_{\boldsymbol{\theta}=\boldsymbol{\theta}_0}$ (c) $\partial_{\theta_2} R(\boldsymbol{\theta}; \boldsymbol{\theta}_0)|_{\boldsymbol{\theta}=\boldsymbol{\theta}_0}$

FIGURE 1. Plots on the surface given by (2.20) of (a) the regular part $R(\boldsymbol{\theta}_0; \boldsymbol{\theta}_0)$ along with the two components of $\nabla R|_{\boldsymbol{\theta}=\boldsymbol{\theta}_0}$ in (b),(c). The parameters are $D = 0.7$, $k = 0.6$, $c = 0.3$.

2.2. **Asymptotic analysis of quasi-equilibrium one-spot solution.** We now proceed with an asymptotic construction of a quasi-equilibrium solution to (1.2) consisting of one spot localized near an $\mathcal{O}(\varepsilon)$ region around $\boldsymbol{\theta}_0(\varepsilon^2 t)$. We then derive an expression for $\dot{\boldsymbol{\theta}}_0$, the slow evolution of the center of the spot. To begin, near $\boldsymbol{\theta}_0$, we let

$$v(\boldsymbol{\theta}, t) = \frac{\sqrt{D}}{\varepsilon} V(\mathbf{y}(\boldsymbol{\theta}), t)\,, \quad u(\boldsymbol{\theta}, t) = \frac{\varepsilon}{A\sqrt{D}} U(\mathbf{y}(\boldsymbol{\theta}), t)\,; \qquad \mathbf{y}(\boldsymbol{\theta}) \equiv \frac{1}{\varepsilon}\mathbf{x}(\boldsymbol{\theta})\,, \tag{2.21}$$

where $\mathbf{x}(\boldsymbol{\theta})$ is the inverse of the Riemannian coordinate system centered at $\boldsymbol{\theta}_0$ defined in (2.13). Note that the $\boldsymbol{\theta}_0$ is a parameter in the map, and thus $\mathbf{x}$ is a function of $\boldsymbol{\theta}_0$; in particular, $\mathbf{x}(\boldsymbol{\theta}_0) = \mathbf{0}$. In the $\mathbf{y}$ coordinates, retaining up to $\mathcal{O}(\varepsilon)$ terms, and assuming that $\tau U_t \ll \mathcal{O}(\varepsilon^{-1})$, the system (1.2) transforms to

$$V_t = \Delta_{\mathbf{y}} V - V + UV^2 \tag{2.22a}$$

$$0 = \Delta_{\mathbf{y}} U - UV^2 - \varepsilon \mathbf{b} \cdot \nabla_{\mathbf{y}} U + \frac{\varepsilon A}{\sqrt{D}} \frac{1}{\sqrt{|g(\boldsymbol{\theta}_0)|}}\,, \tag{2.22b}$$

We show below that, with $u \sim \mathcal{O}(1)$ in the outer region, $A \sim \mathcal{O}(\varepsilon|\log\varepsilon|)$ and thus $\varepsilon A \ll \varepsilon$ so that the last term in (2.22b) does not enter at $\mathcal{O}(\varepsilon)$. The vector $\mathbf{b}$ is defined in terms of the original advection term $\mathbf{c}$ by

$$\mathbf{b}(\mathbf{y}) = \frac{1}{D}\left(\frac{D\boldsymbol{\theta}}{D\mathbf{x}}\right)^{-1} \mathbf{c}(\boldsymbol{\theta}(\varepsilon\mathbf{y}))\,, \tag{2.23}$$

where $\mathbf{c}$ is defined in (1.2).

In (2.22), we expand U and V as

$$U \sim U_0(\rho) + \varepsilon U_1(\mathbf{y})\,, \quad V \sim V_0(\rho) + \varepsilon V_1(\mathbf{y})\,; \qquad \mathbf{y} = \rho \begin{pmatrix} \cos\omega \\ \sin\omega \end{pmatrix}, \quad 0 < \rho < \infty\,, \quad 0 \le \omega < 2\pi\,. \tag{2.24}$$

In (2.24), we have assumed that the leading order spot profile is radially symmetric about its center. Substituting (2.24) into (2.22), we obtain the leading order core problem [28, 8],

$$\Delta_\rho V_0 - V_0 + U_0 V_0^2 = 0\,, \qquad \Delta_\rho U_0 - U_0 V_0^2 = 0\,, \tag{2.25a}$$

$$V_0 \to 0\,, \qquad U_0 \to S\log\rho + \chi(S)\,, \quad \text{as } \rho \to \infty\,, \tag{2.25b}$$

where we have defined the operator $\Delta_\rho \equiv \partial_{\rho\rho} + \rho^{-1}\partial_\rho$. Applying the divergence theorem to the second equation of (2.25a) along with the far-field conditions for U_0 in (2.25b), we compute that the spot strength S satisfies

$$S = \int_0^\infty U_0 V_0^2 \rho d\rho\,, \tag{2.25c}$$

In (2.25b), $\chi(S)$ is a nonlinear function of S that must be computed numerically. In Fig. 2, we show some typical profiles for U_0 and V_0, along with the relationship $\chi(S)$. We note the result from [8] that a single spot is unstable to a self-replication instability when its strength S exceeds $\Sigma_2 \approx 4.31$. This instability is a local instability the analysis of which, to leading order, does not depend on the local curvature or variable potential. In §4, we demonstrate that a slow drift can trigger a self-replication instability.

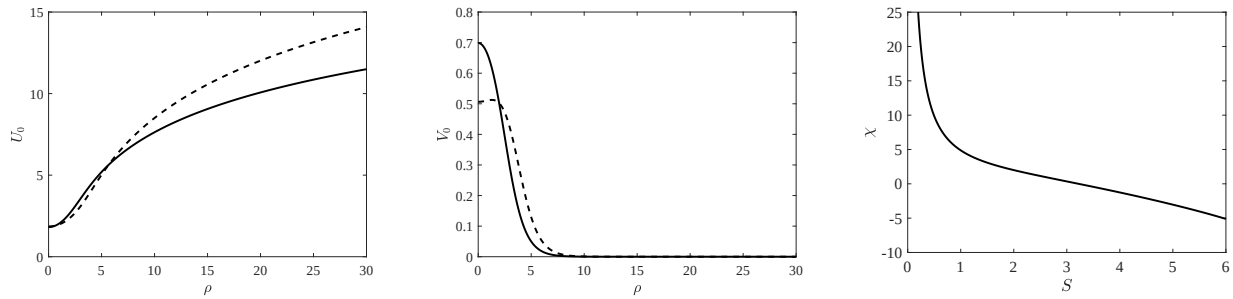

(a) $U_0(\rho)$ (b) $V_0(\rho)$ (c) $\chi(S)$

FIGURE 2. (a) and (b) Numerical solutions of (2.25) for $S \approx 3.92$ (solid) and $S \approx 5.07$ (dashed). As found in [28, 8], the spot profile V_{j0} develops a volcano shape when $S \gtrsim 4.78$. (c) The relationship $\chi(S)$, defined in (2.25b).

To compute the $\mathcal{O}(\varepsilon)$ terms of (2.22), we first compute $\partial_t V_0(\rho)$. Note that $\rho = |\mathbf{y}|$ in (2.24), and $\mathbf{y}$ depends on $\boldsymbol{\theta}_0(\varepsilon^2 t)$ through $\mathbf{y} = \varepsilon^{-1}\mathbf{x}$, where $\boldsymbol{\theta}(\mathbf{x})$ is given by the Riemannian normal coordinates (2.13c). Thus, we have that

$$\partial_t V_0 = V_0'(\rho)\rho_t\,, \qquad \rho_t = \varepsilon \mathbf{e}_\omega \cdot \frac{d\mathbf{x}}{d\sigma}\,; \qquad \mathbf{e}_\omega \equiv \begin{pmatrix} \cos\omega \\ \sin\omega \end{pmatrix}, \qquad \sigma \equiv \varepsilon^2 t\,, \tag{2.26}$$

where ω is defined in (2.24). We thus have, from (2.26) that

$$\partial_t V_0 = \varepsilon V_0'(\rho)\mathbf{e}_\omega \cdot \dot{\mathbf{x}}\,, \qquad \dot{\mathbf{x}} \equiv \frac{d\mathbf{x}}{d\sigma}\,. \tag{2.27}$$

Recalling that $A \ll \mathcal{O}(1)$, we thus have for the $\mathcal{O}(\varepsilon)$ terms of (2.22)

$$\Delta_{\mathbf{y}}\mathbf{W} + M\mathbf{W} = \mathbf{d}\,; \qquad \mathbf{W} \equiv \begin{pmatrix} V_1 \\ U_1 \end{pmatrix}, \quad M \equiv \begin{pmatrix} -1 + 2U_0V_0 & V_0^2 \\ -2U_0V_0 & -V_0^2 \end{pmatrix}, \tag{2.28a}$$

with $\mathbf{d}$ and the far-field conditions conditions given by

$$\mathbf{d} \equiv \begin{pmatrix} V_0'\mathbf{e}_\omega \cdot \dot{\mathbf{x}} \\ U_0'\mathbf{b}(0)\cdot\mathbf{e}_\omega \end{pmatrix}, \qquad \mathbf{W} \sim \begin{pmatrix} 0 \\ -\mathbf{f}\cdot\mathbf{y} + \mathbf{h}\cdot\mathbf{y}\log|\mathbf{y}| \end{pmatrix} \text{ as } |\mathbf{y}| \to \infty\,. \tag{2.28b}$$

Before computing $\mathbf{f}$ in (2.28b), we first remark that, since $U_0' \sim S/\rho$, the nonhomogeneous term $\mathbf{d}$ generates the $\mathbf{h}\cdot\mathbf{y}\log|\mathbf{y}|$ term in the far-field that will be matched by the term proportional to $\boldsymbol{\gamma}$ in (2.3b). We will determine $\mathbf{h}$ in terms of $\boldsymbol{\gamma}$ explicitly below, where we construct the parametrix solution for the Green's function G near $\boldsymbol{\theta}_0$.

The expression for $\mathbf{f}$ will be obtained from matching of the local behavior of the outer solution of u in (1.2b) to the far-field behavior of U in (2.22b). We proceed as in, e.g., [28, 8], and represent, in the sense of distributions, the uv^2 term in (1.2b) as a weighted delta function located at the spot location $\boldsymbol{\theta}_0$. Using (2.21) and (2.25c), we obtain

$$uv^2 \sim \varepsilon\frac{\sqrt{D}}{A}2\pi S\delta(\boldsymbol{\theta};\boldsymbol{\theta}_0)\,. \tag{2.29}$$

With (2.29) in (1.2b), we obtain the leading order outer equation for u,

$$D\Delta_g u - \mathbf{c}(\boldsymbol{\theta})\cdot\nabla u + \frac{1}{\sqrt{|g|}} - \mathcal{V}(\boldsymbol{\theta})u = \varepsilon\frac{\sqrt{D}}{A}2\pi S\delta(\boldsymbol{\theta};\boldsymbol{\theta}_0)\,, \tag{2.30a}$$

with required local behavior obtained from (2.25b),

$$u \sim \frac{\varepsilon}{A\sqrt{D}}\left[\frac{S}{\nu} + S\log|\mathbf{x}| + \chi(S) + \cdots\right] \text{ as } \boldsymbol{\theta} \to \boldsymbol{\theta}_0\,; \qquad \nu \equiv -\frac{1}{\log\varepsilon}\,. \tag{2.30b}$$

In (2.30b), we have recalled the fact that the exponential map of (2.13c) was constructed so that the Euclidean norm, $|\mathbf{x}|$, is equal to the geodesic distance $d_g(\boldsymbol{\theta},\boldsymbol{\theta}_0)$ between $\boldsymbol{\theta}$ and $\boldsymbol{\theta}_0$. With $u \sim \mathcal{O}(1)$ in the outer region, we require the leading order term of (2.30b) to be $\mathcal{O}(1)$, leading to the scaling adopted in [8],

$$A = \frac{\mathcal{A}\varepsilon}{\nu\sqrt{D}}\,, \qquad \mathcal{A} \sim \mathcal{O}(1)\,. \tag{2.31}$$

This scaling leads to the leading order solution for u,

$$u \sim u_c(\boldsymbol{\theta}) - \frac{2\pi\nu S}{\mathcal{A}} G(\boldsymbol{\theta};\boldsymbol{\theta}_0)\,, \tag{2.32a}$$

where $u_c(\boldsymbol{\theta})$ is the solution satisfying the nonhomogeneous elliptic equation

$$-\Delta_g u_c + \frac{1}{D}\mathbf{c}(\boldsymbol{\theta})\cdot\nabla u_c + \frac{1}{D}\mathcal{V}(\boldsymbol{\theta})u_c = \frac{1}{D\sqrt{|g|}}\,, \tag{2.32b}$$

with periodic conditions in $\boldsymbol{\theta}$. Note that, in the special case where $\zeta(\boldsymbol{\theta})$ is a constant (i.e., the surface was flat), we would have $\mathcal{V}\equiv 1$ and $|g|\equiv 1$ for all $\boldsymbol{\theta}$, leading to $u_c \equiv 1$. In (2.32a), $G(\boldsymbol{\theta};\boldsymbol{\theta}_0)$ is the Green's function satisfying (2.3).

In order to match the outer solution $u(\boldsymbol{\theta})$ in (2.32a) to the inner solution constructed in the normal coordinates $\mathbf{x}$, we must write the local behavior of u in terms of $\mathbf{x}$. We thus define

$$u_e(\mathbf{x}) = u(\boldsymbol{\theta}(\mathbf{x}))\,, \quad u_{ce}(\mathbf{x}) = u_c(\boldsymbol{\theta}(\mathbf{x}))\,, \quad R_e(\mathbf{x};\mathbf{0}) = R(\boldsymbol{\theta}(\mathbf{x});\boldsymbol{\theta}_0)\,. \tag{2.33}$$

In (2.33) and below, all functions with the subscript $\cdot_e$ denote quantities that are in terms of the Riemannian normal coordinates $\mathbf{x}$. Using the local behavior of G in (2.3b) along with (2.32a), we obtain the local behavior of the outer solution $u_e(\mathbf{x})$ *in terms of the Riemannian normal coordinates*

$$u_e(\mathbf{x}) \sim \frac{\nu S}{\mathcal{A}}\log|\mathbf{x}| + u_{ce}(\mathbf{0}) - \frac{2\pi\nu S}{\mathcal{A}}R_e(\mathbf{0};\mathbf{0}) - \frac{2\pi\nu S}{\mathcal{A}}\boldsymbol{\gamma}_e\cdot\mathbf{x}\log|\mathbf{x}| + \boldsymbol{\beta}\cdot\mathbf{x}\,, \tag{2.34a}$$

$$\boldsymbol{\beta} \equiv \nabla_{\mathbf{x}}\, u_{ce}(\mathbf{x})\big|_{\mathbf{x}=\mathbf{0}} - \frac{2\pi\nu S}{\mathcal{A}}\nabla_{\mathbf{x}}\, R_e(\mathbf{x};\mathbf{0})\big|_{\mathbf{x}=\mathbf{0}}\,, \tag{2.34b}$$

for some $\boldsymbol{\gamma}_e$ to be computed below. Comparing the leading order terms in (2.34a) and (2.30b), and noting that the $\log|\mathbf{x}|$ terms match by construction, we obtain the matching condition

$$\mathcal{A}u_{ce}(\mathbf{0}) = S\left[1 + 2\pi\nu R_e(\mathbf{0};\mathbf{0})\right] + \nu\chi(S)\,, \tag{2.35a}$$

or equivalently,

$$\mathcal{A}u_c(\boldsymbol{\theta}_0) = S\left[1 + 2\pi\nu R(\boldsymbol{\theta}_0;\boldsymbol{\theta}_0)\right] + \nu\chi(S)\,, \tag{2.35b}$$

which is a nonlinear equation for the spot strength S.

To determine $\mathbf{f}$ in (2.28b), we first begin by computing $\boldsymbol{\gamma}_e$ in (2.34a). To do so, we recall from [52] that the two most singular terms in the expansion of G around $\boldsymbol{\theta}_0$ are contained in leading term of the parametrix

$$Q_0(\mathbf{x}) \equiv \alpha_0(\mathbf{x}) F_0(|\mathbf{x}|)\,. \tag{2.36a}$$

In (2.36a), $\mathbf{x}$ is the normal coordinate, $F_0(r) = (2\pi)^{-1}K_0(r)$ is the zeroth order modified Bessel function of the second kind, and $\alpha_0(\mathbf{x})$ the smooth function on $\mathbb{R}^2$ given explicitly by (cf. (2.19) of [52]),

$$\alpha_0(\mathbf{x}) = |\hat{g}(\mathbf{x})|^{-1/4}|\hat{g}(\mathbf{0})|^{1/4}\exp\left(\int_0^1 \frac{x^j \hat{g}_{jk}(\mathbf{0})b^k(t\mathbf{x})}{2}dt\right)\,; \quad \mathbf{x} \equiv \begin{pmatrix} x^1 \\ x^2 \end{pmatrix}\,, \quad \mathbf{b}(\mathbf{x}) \equiv \begin{pmatrix} b^1(\mathbf{x}) \\ b^2(\mathbf{x}) \end{pmatrix}\,. \tag{2.36b}$$

Recalling that $|\hat{g}(\mathbf{x})| \sim 1 + \mathcal{O}(|\mathbf{x}|^2)$, and with

$$F_0(\mathbf{x}) \sim -(2\pi)^{-1}\log|\mathbf{x}|\,, \qquad \alpha_0(\mathbf{x}) \sim 1 + \mathbf{x}\cdot\nabla_{\mathbf{x}}\,\alpha_0(\mathbf{x})|_{\mathbf{x}=\mathbf{0}}\,, \tag{2.37}$$

a simple calculation yields that

$$\boldsymbol{\gamma}_e = -\frac{1}{4\pi}\mathbf{b}(\mathbf{0})\,. \tag{2.38}$$

Having obtained $\boldsymbol{\gamma}_e$ explicitly, we now proceed with the higher order matching of the inner and outer solutions of u by substituting $\mathbf{x} = \varepsilon\mathbf{y}$ into (2.34a) to obtain

$$u_e(\varepsilon\mathbf{x}) \sim \frac{\nu S}{\mathcal{A}}\log|\varepsilon\mathbf{x}| + u_{ce}(\mathbf{0}) - \frac{2\pi\nu S}{\mathcal{A}}R_e(\mathbf{0};\mathbf{0}) - \varepsilon\frac{2\pi\nu S}{\mathcal{A}}\boldsymbol{\gamma}_e\cdot\mathbf{y}\log|\mathbf{y}| + \varepsilon\boldsymbol{\alpha}\cdot\mathbf{y}\,, \tag{2.39a}$$

where $\boldsymbol{\alpha}$ is given in terms of $\boldsymbol{\beta}$ in (2.34b) and $\boldsymbol{\gamma}_e$ in (2.38) by

$$\boldsymbol{\alpha} \equiv \frac{2\pi S\boldsymbol{\gamma}_e}{\mathcal{A}} + \boldsymbol{\beta}\,. \tag{2.39b}$$

With the scaling of (2.21), we compare far-field behavior of U_1 defined in (2.28b) to the local behavior of $u_e(\mathbf{x})$ in (2.39a) to determine $\mathbf{f}$ and $\mathbf{h}$ of (2.28b),

$$\mathbf{f} = -\frac{\mathcal{A}}{\nu}\boldsymbol{\alpha}\,, \qquad \mathbf{h} = \frac{1}{2}S\mathbf{b}(\mathbf{0})\,. \tag{2.40}$$

We remark that there are three contributions to $\mathbf{f}$ in (2.40). The first contribution is from the term proportional to $\boldsymbol{\gamma}_e$, which arises due to the presence of the advection term $\mathbf{c}(\boldsymbol{\theta})$ in (1.2b). The second contribution is from the $\nabla_{\mathbf{x}}u_{ce}$ term from $\boldsymbol{\beta}$ in (2.34b), which is due to the spatially variable potential along with the (effective) spatially variable background feed. Both of these terms are $\mathcal{O}(\nu^{-1}) \gg \mathcal{O}(1)$. The third and final contribution is from the $\nabla_{\mathbf{x}}R_e$ term in (2.34b). This is an $\mathcal{O}(1)$ term, and is where the effect of surface curvature enters the dynamics. This term also encodes higher order effects of the aforementioned advection and variable potential.

Before relating $\dot{\mathbf{x}}$ to $\mathbf{f}$, we first note that the expression for $\mathbf{h}$ in (2.40) matches exactly the far-field behavior of U_1 generated by the nonhomogeneous term $\mathbf{d}$ in (2.28). To see this, first observe that $V_0 \to 0$ exponentially and $U_0' \to S/\rho$ as $|\mathbf{y}| \to \infty$. Thus, in the far-field, $U_1 \sim U_1^f$, with U_1^f satisfying

$$\Delta_{\mathbf{y}} U_1^f = S\mathbf{b}(\mathbf{0}) \cdot \mathbf{e}_\omega \frac{1}{\rho}\,, \tag{2.41}$$

the solution of which is given by

$$U_1^f = S\mathbf{b}(\mathbf{0}) \cdot \mathbf{e}_\omega \frac{1}{4}\rho\,[2\log\rho - 1]\ . \tag{2.42}$$

Recalling that $\mathbf{y} = \rho\mathbf{e}_\omega$, where $\mathbf{e}_\omega$ is the unit vector given in (2.26), we find that the coefficient of $\mathbf{y}\log|\mathbf{y}|$ is $S\mathbf{b}(\mathbf{0})/2$, indeed agreeing with $\mathbf{h}$ given in (2.40).

To determine $\dot{\mathbf{x}}$, we proceed as in, e.g., [59, 28], and apply a solvability condition on the nonhomogeneous terms in (2.28). To do so, we consider the homogeneous adjoint problem to (2.28), given by

$$\Delta_{\mathbf{y}}\mathbf{W}^\dagger + M^T\mathbf{W}^\dagger = \mathbf{0}\,, \qquad \mathbf{W}^\dagger \equiv \begin{pmatrix} V^\dagger \\ U^\dagger \end{pmatrix}. \tag{2.43}$$

Noting that homogeneous forward problem yields at least two nontrivial solutions corresponding to the translation modes $\partial_{y^j}(V_0, U_0)^T$, $j = 1, 2$, (2.43) must also have a nontrivial null space of dimension at least two. We write these two solutions as

$$\mathbf{P}_c = \mathbf{P}(\rho)\cos\omega\,, \qquad \mathbf{P}_s = \mathbf{P}(\rho)\sin\omega\,; \qquad \mathbf{P} \equiv \begin{pmatrix} P_1 \\ P_2 \end{pmatrix}, \tag{2.44a}$$

where $\mathbf{P}(\rho)$ satisfies

$$\Delta_1\mathbf{P} + M^T\mathbf{P} = \mathbf{0}\,, \quad \mathbf{P} \sim \begin{pmatrix} 0 \\ 1/\rho \end{pmatrix} \text{ as } \rho \to \infty\,; \qquad \Delta_1 \equiv \partial_{\rho\rho} + \frac{1}{\rho}\partial_\rho - \frac{1}{\rho^2}\,. \tag{2.44b}$$

We note that imposing the normalizing $1/\rho$ far-field condition for P_2 uniquely defines $\mathbf{P}$.

We next multiply (2.28a) by $\mathbf{P}_c^T$ and integrate over Ω_r, the disk of radius r centered at the origin in the y^1-y^2 plane. By Green's identity, we obtain

$$\int_{\partial\Omega_R} \mathbf{P}_c^T\partial_n\mathbf{W} - \mathbf{W}^T\partial_n\mathbf{P}_C\, dS_{\mathbf{y}} = \int_{\Omega_r} \mathbf{P}_c^T\mathbf{d}\, d\Omega_{\mathbf{y}}\,. \tag{2.45a}$$

In (2.45a), $\partial\Omega_r$ denotes the boundary of Ω_r, and ∂_n denotes the outward normal derivative. As $r \to \infty$, the limiting behavior of the terms in the first integral are given by

$$\mathbf{P}_c \sim \begin{pmatrix} 0 \\ 1/\rho \end{pmatrix}\cos\omega\,, \qquad \partial_n\mathbf{P}_c \sim \begin{pmatrix} 0 \\ -1/\rho^2 \end{pmatrix}\cos\omega \tag{2.45b}$$

$$\mathbf{W} \sim \begin{pmatrix} 0 \\ \frac{\mathcal{A}}{\nu}\boldsymbol{\alpha}\cdot\mathbf{e}_\omega r + \frac{1}{2}S\mathbf{b}(\mathbf{0})\cdot\mathbf{e}_\omega r\log r \end{pmatrix}, \qquad \partial_n\mathbf{W} \sim \begin{pmatrix} 0 \\ \frac{\mathcal{A}}{\nu}\boldsymbol{\alpha}\cdot\mathbf{e}_\omega + \frac{1}{2}S\mathbf{b}(\mathbf{0})\cdot\mathbf{e}_\omega\,(\log r + 1) \end{pmatrix} \tag{2.45c}$$

where we have used (2.44) to obtain (2.45b), and (2.28b) and (2.40) to obtain (2.45c).

The right-hand side of (2.45a) may be split into two radial integrals as

$$\int_{\Omega_r} \mathbf{P}_c^T \mathbf{d}\, d\Omega_{\mathbf{y}} = \pi \dot{x}_1 \int_0^r P_1 V_0' \rho d\rho + \pi b^1(\mathbf{0}) \int_0^r P_2 U_0' \rho d\rho\,. \tag{2.46a}$$

Integrating by parts on the third integral of (2.46a) and computing the left-hand side of (2.45a) using (2.45b)-(2.45c), we obtain

$$2\pi \frac{A}{\nu}\alpha_1 + \frac{\pi}{2} S b^1(\mathbf{0})\,[2\log r + 1] = \pi \dot{x}_1 \int_0^r P_1 V_0' \rho d\rho + \pi b^1(\mathbf{0}) \left[S \log r - \int_0^r (U_0 - \chi(S))(P_2\rho)'\, d\rho \right] \tag{2.46b}$$

Note that, as a consequence of the $\mathbf{y}\log|\mathbf{y}|$ terms matching in the inner and outer regions, the terms proportional to $\log r$ in (2.46b) cancel. Thus, in the limit that $r \to \infty$, we obtain the ODE for $\dot{x}_1$

$$-\dot{x}_1 = \frac{-2\frac{\mathcal{A}}{\nu}\alpha_1 - \frac{1}{2} S b^1(\mathbf{0}) - \kappa_2 b^1(\mathbf{0})}{\kappa_1}\,, \tag{2.47a}$$

$$\kappa_1(S) \equiv \int_0^\infty P_1 V_0' \rho\, d\rho\,, \qquad \kappa_2(S) \equiv \int_0^\infty (U_0 - \chi(S))(P_2\rho)'\, d\rho\,, \tag{2.47b}$$

where we have used for $\kappa_2(S)$ the fact that $\int_0^\infty (P_2\rho)'\, d\rho = 1$. We remark that the definitions for κ_1 and κ_2 are the same as those given in [59] for the motion of a single spot on the (flat) unit disk. We plot them in Fig. 3 for completeness; note that $\kappa_1 < 0$ for all S below the splitting threshold.

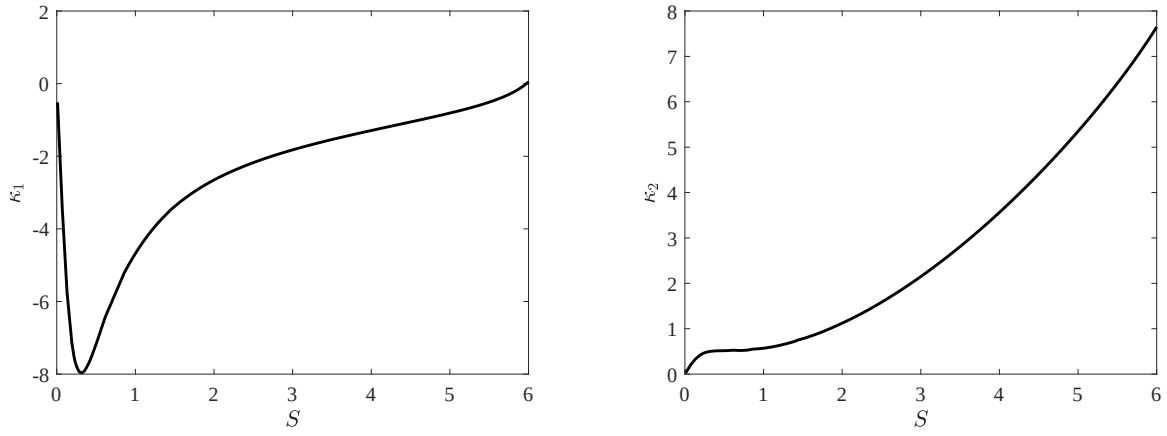

(a) $\kappa_1(S)$ (b) κ_2

FIGURE 3. Plots of (a) $\kappa_1(S)$ and (b) $\kappa_2(S)$ as defined in (2.47b). Note that a spot with strength $S \gtrsim 4.31$ is unstable to a self-replication instability.

Repeating the procedure from (2.45a)-(2.47a) by imposing orthogonality with respect to $\mathbf{P}_s$ yields an analogous expression for $\dot{x}_2$. In vector form, we have for $\dot{\mathbf{x}} = (\dot{x}_1, \dot{x}_2)^T$

$$-\dot{\mathbf{x}} = \frac{1}{\kappa_1}\left[\left(\frac{S}{\nu} - \frac{S}{2} - \kappa_2 \right) \mathbf{b}(\mathbf{0}) - 2\frac{\mathcal{A}}{\nu} \nabla_{\mathbf{x}}\, u_{ce}(\mathbf{x})\big|_{\mathbf{x}=\mathbf{0}} + 4\pi S \nabla_{\mathbf{x}}\, R_e(\mathbf{x};\mathbf{0})\big|_{\mathbf{x}=\mathbf{0}} \right]. \tag{2.48}$$

All quantities in (2.48) are given in terms of the normal coordinates $\mathbf{x}$. We now revert (2.48) back to an expression for $\dot{\boldsymbol{\theta}}_0$ in terms of quantities involving the original $\boldsymbol{\theta}$ coordinates.

For the $\nabla_{\mathbf{x}} u_{ce}$ term in (2.48), the chain rule gives

$$\nabla_{\mathbf{x}} u_{ce}(\boldsymbol{\theta}(\mathbf{x})) = \left(\frac{D\boldsymbol{\theta}}{D\mathbf{x}}\right)^T \nabla u_c(\boldsymbol{\theta})\,, \tag{2.49}$$

where ∇ in (2.49) is the flat gradient in the $\boldsymbol{\theta}$ variables, and $D\boldsymbol{\theta}/D\mathbf{x}$ is the Jacobian matrix defined in (2.15). At $\mathbf{x} = \mathbf{0}$ (i.e., $\boldsymbol{\theta} = \boldsymbol{\theta}_0$), we have that $D\boldsymbol{\theta}/D\mathbf{x} = P(\boldsymbol{\theta}_0)\Lambda^{-1/2}(\boldsymbol{\theta}_0)$, where P and Λ are, respectively, the orthogonal and diagonal matrices defined in (2.6). Thus, at $\mathbf{x} = \mathbf{0}$, (2.49) becomes

$$\nabla_{\mathbf{x}}\, u_{ce}(\boldsymbol{\theta}(\mathbf{x}))|_{\mathbf{x}=\mathbf{0}} = \Lambda^{-1/2} P^T \nabla\, u_c(\boldsymbol{\theta})|_{\boldsymbol{\theta}=\boldsymbol{\theta}_0}\,. \tag{2.50a}$$

In (2.50a), we have dropped the $\boldsymbol{\theta}_0$ arguments in P and Λ for the sake of brevity. Similarly, for the $\nabla_{\mathbf{x}} R_e$ term of (2.48),

$$\nabla_{\mathbf{x}}\, R_e(\boldsymbol{\theta}(\mathbf{x}); \mathbf{0})|_{\mathbf{x}=\mathbf{0}} = \Lambda^{-1/2} P^T \nabla\, R(\boldsymbol{\theta}; \boldsymbol{\theta}_0)|_{\boldsymbol{\theta}=\boldsymbol{\theta}_0}\,. \tag{2.50b}$$

To convert $\mathbf{b}(\mathbf{0})$ back to the original variable $\mathbf{c}$, we use (2.23) to write

$$\mathbf{b}(\mathbf{0}) = D^{-1}\Lambda^{1/2} P^T \mathbf{c}(\boldsymbol{\theta}_0)\,, \tag{2.50c}$$

where D is the diffusivity constant. Lastly, to compute $\dot{\mathbf{x}}$ of (2.48) in terms of $\dot{\boldsymbol{\theta}}_0$, we note the dependence of $\mathbf{x}$ on $\boldsymbol{\theta}_0(\sigma)$ through (2.13c) and compute

$$\dot{\mathbf{x}} = \left.\frac{D\mathbf{x}}{D\boldsymbol{\theta}_0}\right|_{\boldsymbol{\theta}} \dot{\boldsymbol{\theta}}_0\,; \qquad \left.\frac{D\mathbf{x}}{D\boldsymbol{\theta}_0}\right|_{\boldsymbol{\theta}} = \begin{pmatrix} \frac{\partial \mathbf{x}}{\partial \theta_1^0} & \frac{\partial \mathbf{x}}{\partial \theta_2^0} \end{pmatrix}. \tag{2.50d}$$

Now, from (2.13c), we have that $\boldsymbol{\theta} \sim \boldsymbol{\theta}_0 + P\Lambda^{-1/2}\mathbf{x} + \mathcal{O}(\varepsilon)$. Recalling that we require $\dot{\mathbf{x}}$ at $\mathbf{x} = 0$ (i.e., at $\boldsymbol{\theta} = \boldsymbol{\theta}_0$), it follows immediately that

$$\left.\frac{D\mathbf{x}}{D\boldsymbol{\theta}_0}\right|_{\boldsymbol{\theta}=\boldsymbol{\theta}_0} = -\Lambda^{-1/2} P^T\,. \tag{2.50e}$$

Substituting (2.50a)-(2.50e) into (2.48), and noting that $\left(g^{ij}\right) = (g_{ij})^{-1} = P\Lambda^{-1}P^T$, we arrive at the final equation for the slow evolution of the center of a single spot:

$$\frac{d\boldsymbol{\theta}_0}{dt} = \varepsilon^2 \left\{ \frac{1}{\kappa_1 D}\left[\frac{S}{\nu} - \frac{S}{2} - \kappa_2\right] \mathbf{c}(\boldsymbol{\theta}_0) - \frac{2\mathcal{A}}{\nu\kappa_1}\left(g^{ij}(\boldsymbol{\theta}_0)\right) \nabla\, u_c|_{\boldsymbol{\theta}=\boldsymbol{\theta}_0} + \frac{4\pi S}{\kappa_1}\left(g^{ij}(\boldsymbol{\theta}_0)\right) \nabla\, R|_{\boldsymbol{\theta}=\boldsymbol{\theta}_0} \right\} \tag{2.51}$$

We make several remarks regarding (2.51). First, together with (2.35b), this forms a coupled differential-algebraic equation for the location $\boldsymbol{\theta}_0$ and strength S of the spot. Second, we observe that the leading order contributions of advection ($\mathbf{c}(\boldsymbol{\theta}_0)$) and variable potential and source (∇u_c) are $\mathcal{O}(\varepsilon^2\nu^{-1})$. The advection term accounts for the downhill flow of groundwater. Note that, with $\kappa_1 < 0$ in Fig. 3(a), the downhill flow of water acts to transport a spot uphill. Analyses of stripe patterns on sloped terrain (e.g., [25, 45, 48, 47]) has shown that the stripes also move uphill. The ∇u_c term accounts for three spatially dependent effects: the variable rate of evaporation of groundwater due to varying surface exposure, the non-uniform concentration of rainfall reaching the surface, and the accumulation (dispersion) of groundwater at (from) the valley lines (ridge lines). Note that the spatial dependence of all of these three effects stems from the *curvature* of the surface $\mathcal{M}$. Indeed, if $\mathcal{M}$ had no curvature (i.e., a flat surface

with any slope), the surface element $\sqrt{|g|}$ would be a constant, while the mean curvature H in (1.2d) would be equal to 0. In this case, the solution for u_c in (2.32b) would be constant, leading to $\nabla u_c = \mathbf{0}$. As such, we may say that the leading order effect of surface curvature to the spot dynamics is contained in the ∇u_c term, entering at $\mathcal{O}(\varepsilon^2\nu^{-1})$. However, the strength of *curvature-driven* dynamics, such as that computed explicitly for the torus in [52], is a smaller $\mathcal{O}(\varepsilon^2)$ effect and is contained in the ∇R term. This term also contains higher order effects of advection and variable potential. Lastly, we remark that both terms in (2.51) that arise due to the curvature of the surface involve the operator $grad \equiv g^{ij}\partial_j$, the natural definition of the gradient on a surface with metric tensor g_{ij}.

3. Competing effects of advection, spatially varying potential, and curvature

In this section, we discuss the competing effects of downhill advection of groundwater, accumulation at and dispersion from valley lines and ridge lines, respectively, as well as curvature. In Figs. 4(a) - 4(c), we plot the velocity fields of each of the three terms in (2.51) in isolation, while in Fig. 4(d), we plot their sum, which results in the right-hand side of (2.51). The contours correspond to that of the surface specified in (2.20), with yellow (blue) indicating regions of high (low) elevation. In Fig. 4(a), we observe that downhill flow of the water induces an uphill drift of the spot in the direction of steepest increase. Conversely, 4(b) shows that the variable potential tends drive the spot towards the valleys, where there is an accumulation of water due to curvature. Fig. 4(c) plots the vector field of the $\left(g^{ij}(\boldsymbol{\theta}_0)\right)\nabla u_c$ term of (2.51), which encodes the effects of curvature-driven dynamics as well as higher order contributions of advection and variable potential. In Fig. 4(d), the two red curves show the region where the sum of the three velocity fields (i.e., the right-hand side of (2.51)) is small and where the surrounding velocity field points toward it. We emphasize that the red curves do not indicate equilibrium points, but regions toward which spots are attracted and on which they evolve slowly. As we show in §4 below, as $\mathcal{A}$ in (1.2) is increased slowly towards the parameter regime where spots give way to stripe patterns, spots near the red curve are the first ones to coalesce into stripes.

In Figs. 5(a)-5(c), we demonstrate for $\varepsilon = 0.05$, the asymptotic prediction of the differential-algebraic equation (2.51) with (2.35b) for the spot location $\boldsymbol{\theta}_0(t)$ and spot height (heavy solid curve). The open circles are obtained from a finite elements solution of the full PDE system (1.2) using the finite elements software package FlexPDE7 [17], which employs adaptive meshing and timestepping. The dashed curve shows the asymptotic prediction of (2.51) *without* the ∇R term, demonstrating that while this term is $\mathcal{O}(\nu) \ll \mathcal{O}(1)$ with respect to the advection and potential terms in (2.51), its omission leads to the wrong spot path and also the wrong equilibrium location. We remark that the system (2.35b) is highly nonhomogeneous, which causes $\boldsymbol{\theta}(t)$ computed from the finite elements solution to be rather sensitive to both the initial conditions as well as the tolerance of the PDE solver. Our tests showed that the numerical results became closer to the asymptotic results as the tolerance of the solver was tightened; doing so, however, quickly became computationally infeasible. As such, the agreement between the asymptotic prediction and the full numerical solution cannot be expected to agree to an extremely high degree of accuracy. Nevertheless, $\boldsymbol{\theta}_0(t)$ as predicted by (2.51) and (2.35b) deviates from the numerical solution by no more than 0.0364 over the entire duration, while the error in the height never exceeds 7%. In Fig. 5(d), we show snapshots of the spot during its evolution from its initial location near the top of a peak ($t = 0$) to its equilibrium location on the side of the hill ($t \to \infty$). The white curve indicates the path predicted by the asymptotic analysis, showing excellent agreement.

In Fig. 6, for the same parameters but different initial conditions, we demonstrate the reaching of a different stable equilibrium location, at the edge of the (periodic) computational domain. In Fig. 4(d), this location corresponds to the bottom/top of the right red red stripe. The half spots spots as $t \to \infty$ are due to the periodic domain. We remark that a detailed study of the existence and stability of solutions to the nonlinear equation (2.35b) is performed in [8]. In particular, the solution structure consists of two branches on either side of a saddle node; the solutions shown in Figs. 5 and 6 are from the upper branch.

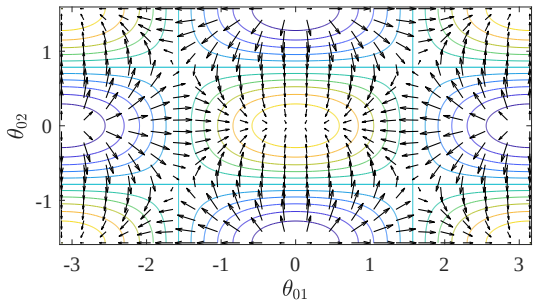

(a) $\mathcal{O}(\varepsilon^2\nu^{-1})$ effect of advection

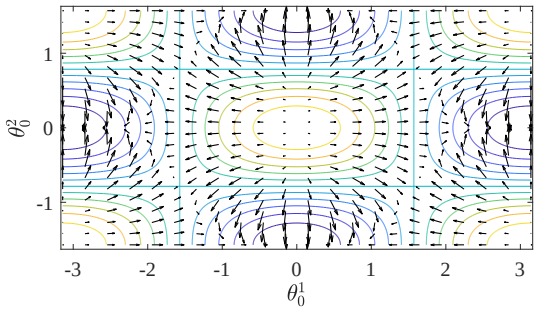

(b) $\mathcal{O}(\varepsilon^2\nu^{-1})$ leading order effect of variable potential

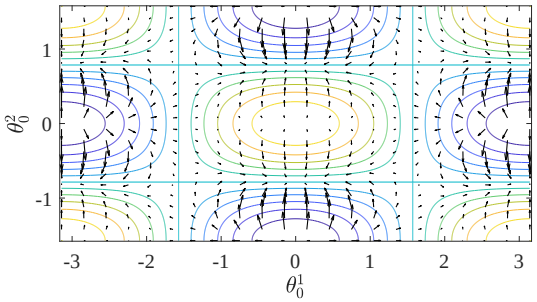

(c) $\mathcal{O}(\varepsilon^2)$ effect of curvature, advection, variable potential

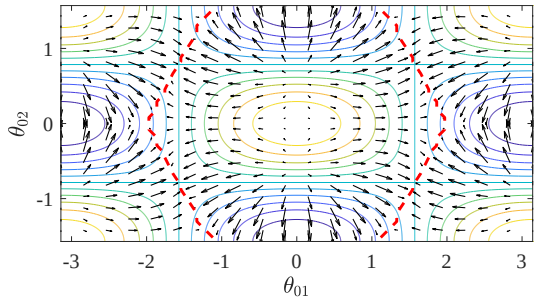

(d) right-hand side of (2.51)

FIGURE 4. The velocity fields corresponding to the terms (a) $\frac{1}{\kappa_1 D}\left[\frac{S}{\nu} - \frac{S}{2} - \kappa_2\right]\mathbf{c}(\boldsymbol{\theta}_0)$, (b) $-\frac{2\mathcal{A}}{\nu\kappa_1}\left(g^{ij}(\boldsymbol{\theta}_0)\right)\nabla\, u_c|_{\boldsymbol{\theta}=\boldsymbol{\theta}_0}$, (c) $\frac{4\pi S}{\kappa_1}\left(g^{ij}(\boldsymbol{\theta}_0)\right)\nabla\, R|_{\boldsymbol{\theta}=\boldsymbol{\theta}_0}$ in (2.51). In (a), the advection term acts to transport a spot uphill in the direction of steepest ascent on the surface. In (b), the variable potential drives the spot toward the valleys where there is an accumulation of water. In (c), the velocity plot is a combination of curvature-driven dynamics along with higher order effects of advection and variable potential. In (d), we plot the sum of the velocity fields of (a)-(c); i.e., the right-hand side of (2.51). The red curves indicate regions toward which spots are attracted and on which they evolve slowly. In the contour plots, yellow (blue) indicates regions of high (low) elevation. The parameter values are $k = 0.6$, $c = 0.3$, $D = 0.7$, $\mathcal{A} = 4.7$, and $\varepsilon = 0.05$.

4. Dynamic triggering of self-replication and the stripe regime

In this section, we show that the slow drift dynamics of a spot can trigger an $\mathcal{O}(1)$ self-replication instability. The splitting results from a drift towards a valley region where water accumulates. In Fig. 7(a), we plot S from the upper branch of the solution to the nonlinear equation (2.35b) for the spot strength S. The parameters are identical to those of Figs. 5 and 6. As the spot drifts according to (2.51), its strength evolves due to the presence of $\boldsymbol{\theta}_0$ in (2.35b). The yellow regions in Fig. 7(a) are regions in which $S(\boldsymbol{\theta}_0) > \Sigma_2 \approx 4.31$, the self-replication threshold. The white arrows indicate the velocity field shown in Fig. 4(d). An initially stable spot located at, for example, $\boldsymbol{\theta}_0 = (0, -\pi/4)$, will undergo a dynamically triggered self-replication instability as it drifts towards $\boldsymbol{\theta}_0 = (0, -\pi/2)$, which would otherwise be a stable equilibrium of (2.51). In Fig. 7(b), we plot snapshots of the single spot quasi-equilibrium as it drifts. At time $t = 198$, a self-replication instability is initiated due to a unstable "peanut-splitting" mode (cf. [8]). After the splitting event, the two spots drift apart and settle in a

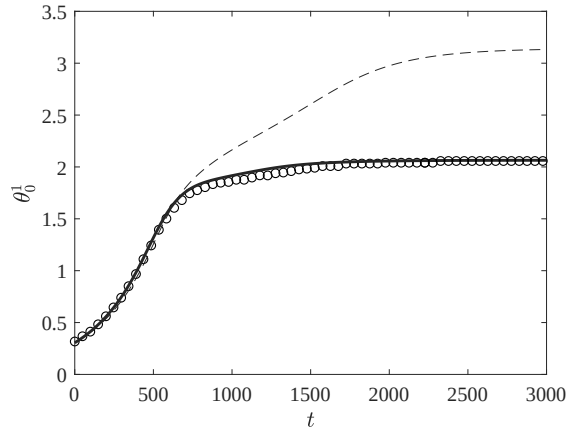

(a) $\theta_0^1(t)$

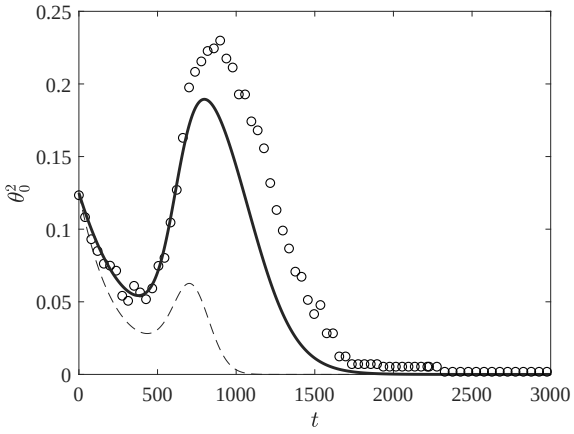

(b) $\theta_0^2(t)$

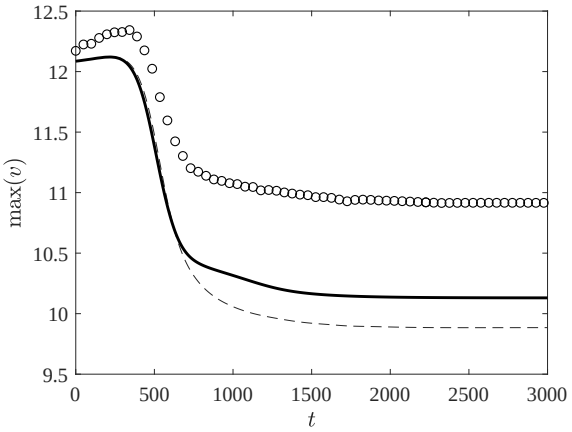

(c) spot height vs. t

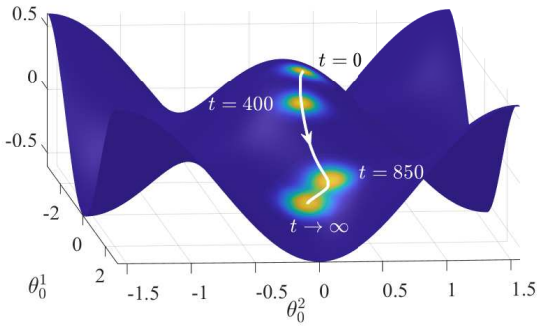

(d) snapshots of spot drift

FIGURE 5. Numerical result (dots) versus asymptotic prediction (solid) from (2.51) of $\boldsymbol{\theta}_0(t) = (\theta_0^1(t), \theta_0^2(t))$ ((a) and (b)) along with the height of the spot (c). The dashed curve in (a)-(c) shows the asymptotic prediction *without* the ∇R term in (2.51), showing that the two leading order $\mathcal{O}(\nu^{-1})$ terms are not enough to accurately predict the spot evolution. (d) Snapshots of the spot on the surface (2.20) at various times during its evolution ($t = 0, 400, 850$, and equilibrium location). The white line indicates the asymptotic prediction. The parameters are $k = 0.6$, $c = 0.3$, $D = 0.7$, $\varepsilon = 0.05$, and $\mathcal{A} = 4.7$.

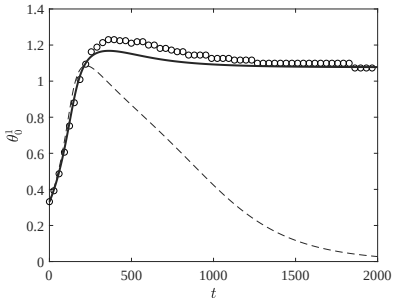

(a) $\theta_0^1(t)$

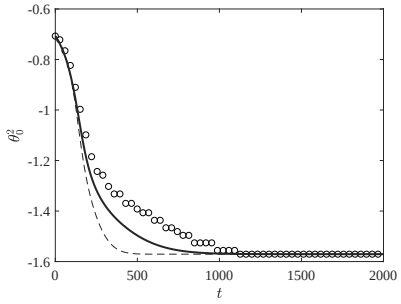

(b) $\theta_0^2(t)$

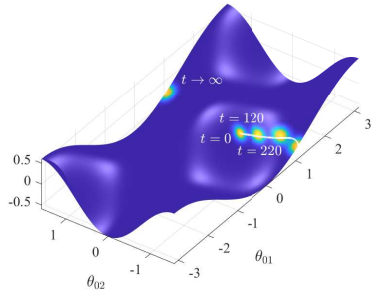

(c) snapshots of spot drift

FIGURE 6. Numerical result (dots) versus asymptotic prediction (solid) from (2.51) of $\boldsymbol{\theta}_0(t) = (\theta_0^1(t), \theta_0^2(t))$ ((a) and (b)). The dashed curves shows the asymptotic prediction *without* the ∇R term in (2.51). (c) Snapshots of the spot on the surface (2.20) at various times during its evolution ($t = 0, 120, 220$, and equilibrium location). The white line indicates the asymptotic prediction, while the half spots as $t \to \infty$ are due to the periodic domain. The parameters are $k = 0.6$, $c = 0.3$, $D = 0.7$, $\varepsilon = 0.05$, and $\mathcal{A} = 4.7$.

two-spot equilibrium configuration. In this case, the splitting direction is orthogonal to the direction of drift.

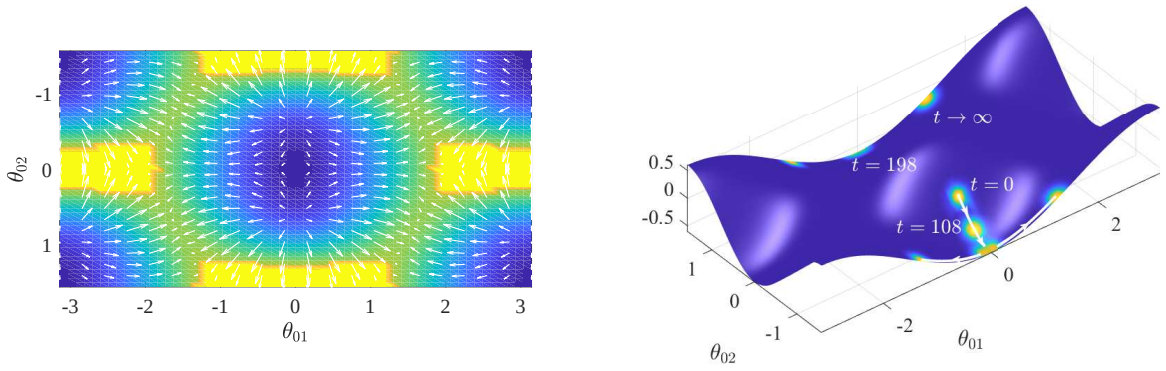

(a) $S(\boldsymbol{\theta}_0)$ (b) snapshots of a splitting event

FIGURE 7. A dynamically triggered self-replication event. (a) A plot of $S(\boldsymbol{\theta}_0)$; the yellow regions indicate $S(\boldsymbol{\theta}_0) > \Sigma_2 \approx 4.31$. (b) Snapshots of a single spot drifting towards the valley $\boldsymbol{\theta}_0 = (0, -\pi/2)$. At $t = 198$, an instability is triggered as the spot enters a region in which the spot strength S exceeds Σ_2. The spots then drift apart, reaching an equilibrium configuration as $t \to \infty$. The half-spots are due to the periodic domain. The parameters are $k = 0.6$, $c = 0.3$, $D = 0.7$, $\varepsilon = 0.05$, and $\mathcal{A} = 4.7$.

Self-replication instabilities may also be triggered through a slow increase in $\mathcal{A}$, the rate of rainfall. A detailed study of this phenomenon was done in [53] for 3-D spot patterns in the sphere in which successive splitting events resulted from a slow linear ramp of the feed-rate parameter, leading to a slow increase in the number of spots. As this linear ramp continues, we expect stripe-like structures to form as $\mathcal{A}$ increases into the "stripe regime"; in the case of a flat rectangular domain, a homoclinic stripe can be constructed by extending a one-dimensional spike trivially in the transverse direction (see [23]). As such, for our generalized Gray-Scott model (1.2b), we expect the stripe regime to correspond to the 1-D spike regime. Three distinct spike regimes were identified in [39] for the Gray-Scott model: the low feed-rate regime $\mathcal{A} \sim \mathcal{O}(\varepsilon^{-1/2}\nu)$ analyzed in [26], the intermediate feed-rate regime $\mathcal{O}(\varepsilon^{-1/2}\nu) \ll \mathcal{A} \ll \mathcal{O}(\varepsilon^{-1}\nu)$ analyzed in [13, 14], and the high feed-rate regime $\mathcal{A} \sim \mathcal{O}(\varepsilon^{-1}\nu)$, analyzed in [27]. In Fig. 8, we perform a slow ramp in $\mathcal{A}$ to demonstrate the transition from a localized spot pattern to the initial formation of stripe-like structures, and finally to full vegetation coverage.

In Fig. 8(a), we show a spot pattern that is near "saturation"; i.e., the next splitting event resulting from an increase in $\mathcal{A}$ will not result in the formation of two separate spots, but instead in the coalescing of spots into stripe-like structures. In Fig. 8(b), we show the resulting stripe-like structures that form near the two red curves of Fig. 4(d), which indicate regions where the velocity field of a one-spot pattern is small and where the surrounding velocity field points toward it. In Fig. 8(c), we observe that an increase in $\mathcal{A}$ results in a largely uniform vegetation coverage with the exception of the steep sloped regions; this is due to the nature of our model, which assumes that these regions receive lower per unit area rainfall. In Fig. 8(d), we show that a further increase in $\mathcal{A}$ leads to these spots coalescing into stripe-like structures before the surface reaches near-uniform vegetation coverage (not shown).

5. DISCUSSION

Based on that introduced in [18], we have proposed a reaction-advection-diffusion model for vegetation density and soil water concentration on an arbitrary terrain with elevation given by $z = \zeta(\theta_1, \theta_2)$. Our model involves operators and quantities that account for the geometry of the surface, allowing for a coordinate-free formulation. While we make no claim regarding the physical accuracy of our model in

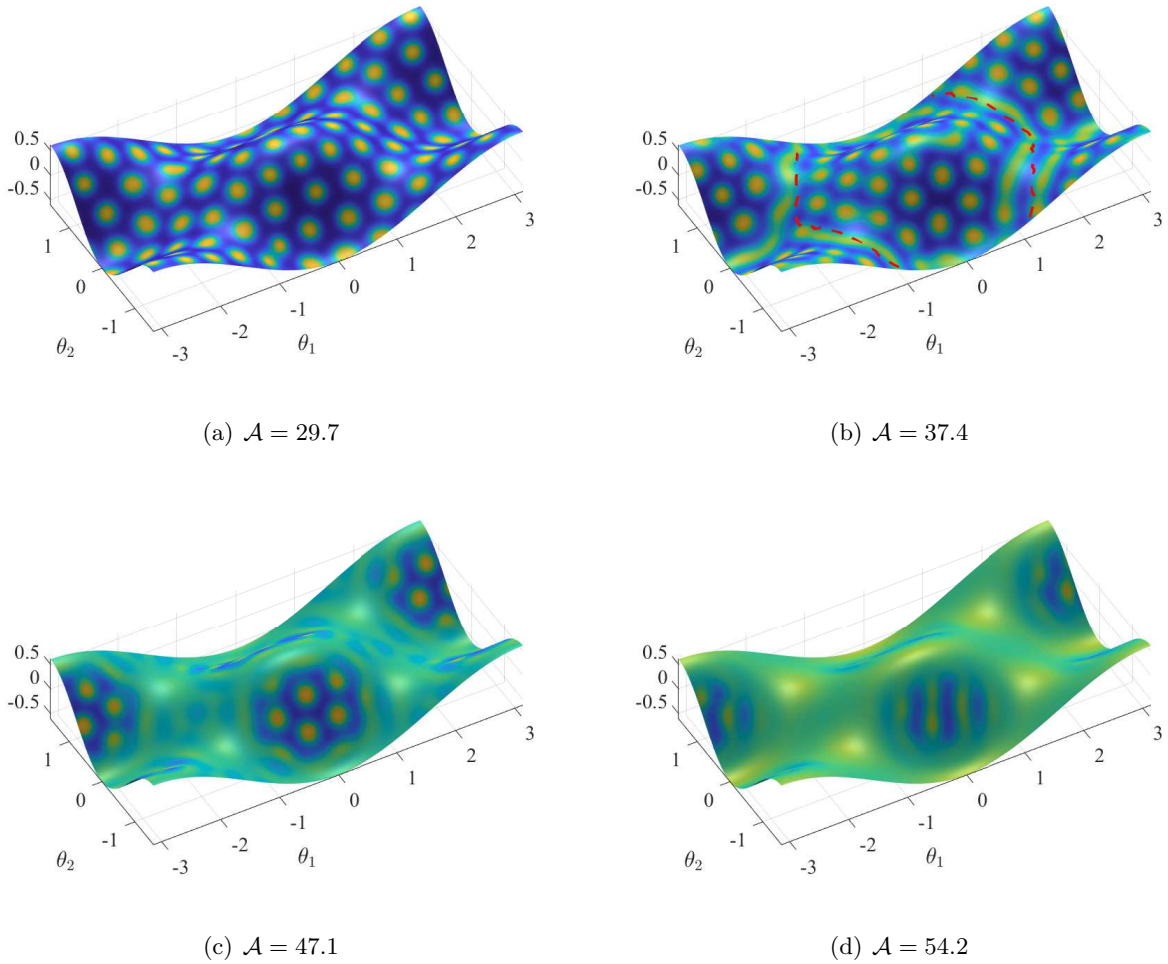

(a) $\mathcal{A} = 29.7$

(b) $\mathcal{A} = 37.4$

(c) $\mathcal{A} = 47.1$

(d) $\mathcal{A} = 54.2$

FIGURE 8. Evolution of a spot pattern under a slow linear increase in $\mathcal{A}$. (a) Nearly "saturated" spot pattern; the next splitting event will begin the process of spots coalescing into stripe-like structures. (b) Stripe-like structures beginning to form near the two red curves of Fig. 4(d). (c) A largely uniform coverage state with the exception of the sloped regions due to a lower per unit area rainfall. (d) The spots on the slopes coalescing into stripes before the surface reaches near-uniform vegetation coverage (not shown).

comparison to that of [18], we submit that it leads to a more natural formulation from a geometric perspective for physical systems involving diffusive and advective transport on a curved surface. In contrast to that of Gandhi et al., the system takes account only of the intrinsic geometry of the surface $\mathcal{M}$ modulo a vector field transverse to the surface which accounts for the vertical direction of rainfall. The resulting model can be viewed as generalized Gray-Scott model, with spatially varying advection, potential, and feed-rate.

Our primary goal in this work was to demonstrate a method for analysis of localized solutions to a reaction-advection-diffusion system on a curved surface. In particular, upon transforming to Riemannian normal coordinates in the local region of the spot, we performed a matched asymptotic analysis to construct a quasi-equilibrium one-spot solution. We then derived an differential-algebraic equation describing its slow drift on the surface; for a system that includes advection and a spatially variable potential, this analysis is new. The result showed that the presence of advection and variable potential effects lead to an $\mathcal{O}(\varepsilon^2|\log\varepsilon|)$ drift velocity instead of the usual $\mathcal{O}(\varepsilon^2)$ velocity observed in the absence of these effects [8]. We further showed that higher order effects of advection and variable potential, along with effects of surface curvature, arise at $\mathcal{O}(\varepsilon^2)$, and are encoded in the gradient of the regular part of a certain Green's function. Numerical tests confirmed that this higher order effect must be included in order to accurately predict the spot's motion.

To compute the gradient of the Green's function, we employed a generalization of the analytic-numerical method first developed in [52] for a simpler Green's function on the surface of a torus. This method allowed for the computation of a Green's function of a general second order linear operator on a general surface, allowing us to account for a spatially varying advection as well as spatially varying potential. Accurately computing this Green's function, in particular, the gradient of its regular part, was the key to accurately predicting the spot's motion.

While the analytic methods that we have used here are conducive to the study of localized spot patterns, it would be interesting to develop techniques for the study of localized stripe patterns on curved surfaces. The computational results of [18] indicate that vegetation stripes may arc according to contours of the terrain. It would also be interesting to understand how human pressures such as woodcutting and systematic grazing [4, 1], or natural terrain features such as preferential water flow paths [1, 37], may impact the behavior of patterns. To analyze such features may require the detailed computation of certain Green's functions on domains containing small holes or cracks. Lastly, we remark that the utility of our analytic-numerical method for computing Green's functions extends beyond applications in pattern formation. For example, analysis of the narrow escape problem on the surface of the unit sphere was solved using a known formula for the Green's function for the sphere [10]. On an arbitrary surface, with anisotropic diffusion or advection, explicit formulae for the Green's function may not exist. Our analytic-numerical method offers a way forward for analysis of these more complex problems.

Acknowledgments

The second author was supported by Grants ARC DP190103451 and ARC DP190103302.

Appendix A. Rescaling of (1.1) and its coordinate-free form (1.3)

We first demonstrate the rescaling of (1.1) that leads to (1.2). We first divide by (1.1a) by a, the rate of per unit area rainfall (in the X-Y plane), and divide (1.1b) by m, the rate of plant death, to obtain

$$\frac{1}{\tilde{m}}V_t = \frac{\tilde{D}_V}{\tilde{m}}\Delta_{\tilde{g}}V - V + \frac{1}{\tilde{m}}UV^2\,, \qquad t>0\,, \quad (X,Y)\in[0,L_X]\times[0,L_Y]\,, \tag{A.1a}$$

$$\frac{1}{a}U_t = \frac{\tilde{D}_U}{a}\Delta_{\tilde{g}}U + \frac{1}{a}\,\mathrm{div}_{\tilde{g}}(\tilde{\mathbf{c}}U) + \frac{1}{\sqrt{|\tilde{g}|}} - \frac{\tilde{p}}{a}\sqrt{|\tilde{g}|}U - \frac{1}{a}UV^2\,, \qquad t>0\,, \quad (X,Y)\in[0,L_X]\times[0,L_Y]\,. \tag{A.1b}$$

We then let $mt\to t$ and $(\tilde{p}/a)U\to u$, leading to

$$V_t = \frac{\tilde{D}_V}{\tilde{m}}\Delta_{\tilde{g}}V - V + \frac{a}{\tilde{p}\tilde{m}}uV^2\,, \tag{A.2a}$$

$$\frac{m}{\tilde{p}}u_t = \frac{\tilde{D}_U}{\tilde{p}}\Delta_{\tilde{g}}u + \frac{1}{\tilde{p}}\,\mathrm{div}_{\tilde{g}}(\tilde{\mathbf{c}}u) + \frac{1}{\sqrt{|\tilde{g}|}} - \sqrt{|\tilde{g}|}u - \frac{1}{\tilde{p}}uV^2\,. \tag{A.2b}$$

Next, we let $V\to\sqrt{\tilde{p}}v$, which results in

$$v_t = \frac{\tilde{D}_V}{\tilde{m}}\Delta_{\tilde{g}}v - v + \frac{a}{\tilde{m}}uv^2\,, \tag{A.3a}$$

$$\frac{m}{\tilde{p}}u_t = \frac{\tilde{D}_U}{\tilde{p}}\Delta_{\tilde{g}}u + \frac{1}{\tilde{p}}\mathrm{div}_{\tilde{g}}(\tilde{\mathbf{c}}u) + \frac{1}{\sqrt{|\tilde{g}|}} - \sqrt{|\tilde{g}|}u - uv^2\,. \tag{A.3b}$$

We then rescale the spatial variables X and Y as $(X,Y)\to(2\pi)^{-1}L_x(\theta_1,\theta_2)$ so that $(\theta_1,\theta_2)\in(0,2\pi)\times(0,2\pi L_Y/L_X)$. Lastly, we rename $2\pi L_Y/L_X\to L_{\theta_2}$, $\tilde{m}/\tilde{p}\to\tau$, $(2\pi/L_X)^2\tilde{D}_U/\tilde{p}\to D$, $\tilde{\mathbf{c}}/\tilde{p}\to\mathbf{c}$, $a/\tilde{m}\to A$, $(2\pi/L_X)^2\tilde{D}_V/m\to\varepsilon^2$, $\tilde{g}\to g$, and expand the $\mathrm{div}_g(\tilde{\mathbf{c}}u)$ term to arrive at (1.2).

We now give a simple physical motivation for the form of the velocity vector $\tilde{\mathbf{c}}$ in (1.1c). Consider a mass moving down an inclined plane of angle ϕ with respect to the horizontal. In the limit where high drag proportional to velocity dominates the inertial term, the velocity of the object is proportional to $\sin\phi$. On a surface with level curves $\tilde{\zeta}(X,Y) = k$, the mass travels in the direction opposite $\nabla\tilde{\zeta}$ in the X-Y plane. Considering the embedding of the surface in $\mathbb{R}^3$, the unit vector $\hat{n}$ pointing in the direction of velocity is then

$$\hat{\mathbf{n}} = -\frac{1}{|\nabla\tilde{\zeta}|\sqrt{1+|\nabla\tilde{\zeta}|^2}}(\nabla\tilde{\zeta}, |\nabla\tilde{\zeta}|^2)\,; \qquad \nabla\tilde{\zeta} = (\tilde{\zeta}_X, \tilde{\zeta}_Y)\,. \tag{A.4}$$

On the other hand, the sine of the angle ϕ that $\hat{n}$ makes with the X-Y plane is given by

$$\sin\phi = \frac{|\nabla\tilde{\zeta}|}{\sqrt{1+|\nabla\tilde{\zeta}|^2}}\,. \tag{A.5}$$

The velocity vector $\tilde{\mathbf{v}}$ in $\mathbb{R}^3$ must then given by $\tilde{\mathbf{v}} = \tilde{c}\,\hat{\mathbf{n}}\sin\phi$, for some positive constant $\tilde{c}$, or, using (A.4) and (A.5),

$$\tilde{\mathbf{v}} = -\tilde{c}\frac{1}{1+|\nabla\tilde{\zeta}|^2}(\nabla\tilde{\zeta}, |\nabla\tilde{\zeta}|^2)\,. \tag{A.6}$$

Since we treat the surface from an intrinsic perspective rather than as an object embedded in $\mathbb{R}^3$, we take for the velocity vector $\tilde{\mathbf{c}}$ the (negative of the) first two components of $\tilde{\mathbf{v}}$, yielding (1.1c). We note that, in the limit $|\nabla\tilde{\zeta}| \to \infty$, $\tilde{\mathbf{c}} \to \mathbf{0}$ as required.

There are two primary reasons for expressing (1.1) in its coordinate-free form (1.3). First, the model that we propose must be independent of the chosen coordinate system, and being able to express (1.1) in the form (1.3) shows that our model is indeed coordinate-invariant.

Coordinate invariance can also be a powerful ally in various calculations. If we know that our model is independent of coordinates, we are free to choose *any* coordinate system in our analyses and computations. This allows us to use convenient coordinate systems which simplify some calculation significantly. This is a common idea in Riemannian geometry which we repeatedly use in this article when performing computations in geodesic coordinates.

To see that (1.3) is indeed the coordinate-free expression of (1.1), we actually choose a coordinate system for which (1.1) is the expression of (1.3) in this particular coordinate system. For a reference on differential geometry notation and terminology, see [32]. Let P be a plane which meets E orthogonally so that geodesics (straight lines) starting on P in the direction of $-E$ meet $\mathcal{M}$ in positive time. As P endowed with the metric obtained by pulling back the Euclidean metric in $\mathbb{R}^3$ by $\iota_{\mathcal{M}}$ is isometric to $\mathbb{R}^2$ (with Euclidean metric), we can choose a global isometry $(X,Y) : P \to \mathbb{R}^2$ which now acts as a coordinate system on P. We define a function $\tilde{Z}$ on $\mathbb{R}^3$ by the following procedure. For each point $p \in \mathbb{R}^3$ let $\mathrm{proj}_P(p)$ be the orthogonal projection of p onto the plane P. The point p can then be reached from $\mathrm{proj}_P(p)$ by flowing along the vector field $-E$ after time $\tilde{Z}(p) \in \mathbb{R}$ (allowing for negative time). The functions $(X, Y, \tilde{Z})$ now forms a new coordinate system in $\mathbb{R}^3$ for which

$$E = -\partial_{\tilde{Z}}. \tag{A.7}$$

Note that this is simply a special case of a normal coordinate system for the Euclidean metric along the hyperplane P.

Owing to the fact that E is transverse to $\mathcal{M}$, we can express $\mathcal{M}$ in the $(X, Y, \tilde{Z})$ coordinate as $\{(X, Y, \tilde{Z}) \mid \tilde{Z} = \tilde{\zeta}(X, Y)\}$ for some smooth function ζ. The metric tensor for $\mathbb{R}^3$ in this coordinate is of course $dX^2 + dY^2 + d\tilde{Z}^2$. To compute the coordinate expression for the metric $\tilde{g} = \iota_{\mathcal{M}}(dX^2 + dY^2 + d\tilde{Z}^2)$, we simply substitute $Z = \tilde{\zeta}(X, Y)$ into $d\tilde{Z}^2$ to obtain

$$\tilde{g} = (1 + \tilde{\zeta}_X^2)dX^2 + (1 + \tilde{\zeta}_Y^2)dY^2 + 2\tilde{\zeta}_X\tilde{\zeta}_Y dXdY. \tag{A.8}$$

In these coordinates the unit normal vector to $\mathcal{M}$ is

$$\tilde{\nu} = (1 + \tilde{\zeta}_X^2 + \tilde{\zeta}_Y^2)^{-1/2}(\tilde{\zeta}_X\partial_X + \tilde{\zeta}_Y\partial_Y - \partial_{\tilde{Z}})\,, \tag{A.9}$$

so that

$$|\langle E, \tilde{\nu}\rangle_e| = (1 + \tilde{\zeta}_X^2 + \tilde{\zeta}_Y^2)^{-1/2}. \tag{A.10}$$

We now observe the determinant of the coordinate expression of the metric tensor in (A.8) is given by $|\tilde{g}| = 1 + \tilde{\zeta}_X^2 + \tilde{\zeta}_Y^2$. Therefore, we may replace $|\langle E, \tilde{\nu}\rangle_e|$ in (1.3) by $1/\sqrt{\tilde{g}}$ when expressed in coordinates. Thus we see that (1.1) is just (1.3) in the coordinates $(X, Y, \tilde{Z})$.

To verify that $\tilde{\mathbf{c}} \in T\mathcal{M}$ defined as the unique vector on $\mathcal{M}$ satisfying $D\iota_{\mathcal{M}}\tilde{\mathbf{c}} = E - \langle E, \tilde{\nu}\rangle_e \tilde{\nu}$ is given by (1.1c) in the $(X, Y, \tilde{Z})$ coordinates, observe that $\iota_{\mathcal{M}}$ in these coordinates is given by $\iota_{\mathcal{M}} : (X, Y) \mapsto (X, Y, \tilde{\zeta}(X, Y)$ (recall that $D\iota_{\mathcal{M}}$ is the differential map/pushforward mapping $T\mathcal{M}$ to $T\mathbb{R}^3$). Therefore

$$D\iota_{\mathcal{M}}(a\partial_X + b\partial_Y) = a\partial_X + b\partial_Y + (a\zeta_X + b\zeta_Y)\partial_{\tilde{Z}}.$$

Setting $\tilde{\mathbf{c}} = a\partial_X + b\partial_Y$, the equation $D\iota_{\mathcal{M}}\tilde{\mathbf{c}} = E - \langle E, \tilde{\nu}\rangle_e \nu$ is now given by

$$-(1+\tilde{\zeta}_X^2+\tilde{\zeta}_Y^2)^{-1}(\tilde{\zeta}_X^2+\tilde{\zeta}_Y^2)\partial_Z - (1+\tilde{\zeta}_X^2+\tilde{\zeta}_Y^2)^{-1}\tilde{\zeta}_X\partial_X - (1+\tilde{\zeta}_X^2+\tilde{\zeta}_Y^2)^{-1}\tilde{\zeta}_Y\partial_Y = a\partial_X + b\partial_Y + (a\tilde{\zeta}_X + b\tilde{\zeta}_Y)\partial_Z.$$

This yields $a = -(1 + \tilde{\zeta}_X^2 + \tilde{\zeta}_Y^2)^{-1}\tilde{\zeta}_X$ and $b = -(1 + \tilde{\zeta}_X^2 + \tilde{\zeta}_Y^2)^{-1}\tilde{\zeta}_Y$ which is precisely (1.1c).

We finally remark that that $|\tilde{g}|^{-1}\nabla\tilde{\zeta}\cdot\nabla u = du(d\tilde{\zeta}^\sharp)$, where $\sharp$ denotes the raising of the index by metric tensor $\tilde{g}$, and is simply the inner product between the exterior derivatives of the functions u and $\tilde{\zeta}$ with respect to the metric obtained by pulling back the Euclidean metric by $\iota_{\mathcal{M}}$.

Appendix B. Derivation of $\boldsymbol{\gamma}_e$ in (2.38)

In this appendix, we derive $\boldsymbol{\gamma}_e$ in (2.38), the coefficient of $\mathbf{x}\log|\mathbf{x}|$ in the local behavior of the Green's function G in Riemannian normal coordinates. Here, $\mathbf{x}(\boldsymbol{\theta}) = (x^1(\boldsymbol{\theta}), x^2(\boldsymbol{\theta}))^T$ is the inverse of the Riemannian coordinate system centered at $\boldsymbol{\theta}_0$ defined in (2.13); in particular, $\mathbf{x} = 0$ corresponds to $\boldsymbol{\theta} = \boldsymbol{\theta}_0$, the location of the source. In these coordinates, G satisfying (2.3) has the local behavior

$$G \sim -\frac{1}{2\pi}\log|\mathbf{x}| + \boldsymbol{\gamma}_e\cdot\mathbf{x}\log|\mathbf{x}| + R_e(\mathbf{0};\mathbf{0}) + \mathbf{x}\cdot\nabla_{\mathbf{x}}R_e(\mathbf{0};\mathbf{0})\,, \tag{B.1}$$

where $R_e(\mathbf{x};\mathbf{0}) = R(\boldsymbol{\theta}(\mathbf{x});\boldsymbol{\theta}_0)$. We now seek γ_e of (B.1) in terms of $\mathbf{b}$, which is defined in terms of $\mathbf{c}$ in (2.23). We first recall from §2.3 of [52] that an asymptotic for G near $\mathbf{x} = \mathbf{0}$ is given by

$$G \sim \sum_{j=0}^{N}\alpha_j(\mathbf{x})F_0(|\mathbf{x}|)\,, \tag{B.2}$$

where the coefficients $\alpha_j(\mathbf{x})$ are solutions of transport equations (cf. (2.19) and (2.27) of [52]), and F_j are basis functions satisfying the radially symmetric equations on $\mathbb{R}^2$ (cf. (2.6) of [52])

$$(\Delta + z)F_0 = \delta_0\,, \qquad (\Delta + z)F_j = jF_{j-1}\,, \quad j \geq 1\,. \tag{B.3}$$

In (B.3), Δ is the flat Laplacian with non-positive eigenvalues, $z \in \mathbb{C}\setminus\mathbb{R}_+$ is some parameter chosen so that $\Delta + z$ is invertible on the space of distributions, and $\delta_0 = \delta(x^1)\delta(x^2)$ is the Dirac delta function centered at the origin. From (B.3), we observe that $F_0 = (2\pi)^{-1}K_0(\sqrt{z}|\mathbf{x}|)$ so that

$$F_0 \sim -\frac{1}{2\pi}\log|\mathbf{x}| - \frac{1}{4\pi}\log z + \log 2 - \gamma + \mathcal{O}(|\mathbf{x}|^2\log|\mathbf{x}|)\,, \qquad |\mathbf{x}| \ll 1\,, \tag{B.4}$$

while $F_j \sim |\mathbf{x}|^{2j}\log|\mathbf{x}|$ for $j \geq 1$. Thus, only the $j = 0$ term in (B.2) contributes to $\boldsymbol{\gamma}_e$. It remains then to compute the linear term in the expansion of $\alpha_0(\mathbf{x})$ in (2.36b) near the origin. To proceed, we recall that under the transformation from the original coordinates $\boldsymbol{\theta}$ to the Riemannian normal coordinates $\mathbf{x}$ in (2.13), the leading order behavior of the metric tensor $\hat{g}(\mathbf{x})$ is given by $\hat{g}_{jk}(\mathbf{x}) \sim \delta_{jk} + \mathcal{O}(|\mathbf{x}|^2)$. We thus have

$$\partial_{x^1}\alpha_0(\mathbf{x}) \sim \mathcal{O}(|\mathbf{x}|)\exp\left(\int_0^1 \frac{x^j\delta_{jk}b^k(t\mathbf{x})}{2}dt\right) + \\ + (1 + \mathcal{O}(|\mathbf{x}|^2)\exp\left(\int_0^1 \frac{x^j\delta_{jk}b^k(t\mathbf{x})}{2}dt\right)\int_0^1 \frac{b^1(t\mathbf{x}) + tx^j\delta_{jk}b^k(t\mathbf{x})}{2}dt\,. \tag{B.5}$$

Evaluating $\partial_{x^1}\alpha_0(\mathbf{x})$ at $\mathbf{x}=\mathbf{0}$, we obtain

$$\partial_{x^1}\alpha_0(\mathbf{x})|_{\mathbf{x}=\mathbf{0}} = \frac{1}{2}b^1(\mathbf{0})\,. \tag{B.6a}$$

Similarly,

$$\partial_{x^2}\alpha_0(\mathbf{x})|_{\mathbf{x}=\mathbf{0}} = \frac{1}{2}b^2(\mathbf{0})\,. \tag{B.6b}$$

For $\mathbf{x}$ near the origin, $\alpha_0(\mathbf{x})$ therefore has the expansion

$$\alpha_0(\mathbf{x}) \sim 1 + \frac{1}{2}\mathbf{b}(\mathbf{0})\cdot\mathbf{x}\,. \tag{B.7}$$

Recalling that $G \sim \alpha_0(\mathbf{x})F_0(\sqrt{z}|\mathbf{x}|)$, and using the local behavior of $\alpha_0(\mathbf{x})$ in (B.7) and of $F_0(\sqrt{z}|\mathbf{x}|)$ in (B.4), we obtain (2.38) for $\boldsymbol{\gamma}_e$.

References

[1] J. E. Baartman, A. J. Temme, and P. M. Saco, *The effect of landform variation on vegetation patterning and related sediment dynamics*, Earth Surface Processes and Landforms, 43 (2018), pp. 2121–2135.

[2] R. Barreira, C. M. Elliott, and A. Madzvamuse, *The surface finite element method for pattern formation on evolving biological surfaces*, Journal of mathematical biology, 63 (2011), pp. 1095–1119.

[3] R. Bastiaansen, P. Carter, and A. Doelman, *Stable planar vegetation stripe patterns on sloped terrain in dryland ecosystems*, arXiv preprint arXiv:1811.10226, (2018).

[4] M. l. Berre and L. Messan, *The W region of Niger: Assets and implications for sustainable development*, Nature and Resources (United Kingdom), (1995).

[5] I. Bordeu, M. G. Clerc, P. Couteron, R. Lefever, and M. Tlidi, *Self-replication of localized vegetation patches in scarce environments*, Scientific reports, 6 (2016), p. 33703.

[6] P. Carter and A. Doelman, *Traveling stripes in the Klausmeier model of vegetation pattern formation*, SIAM Journal on Applied Mathematics, 78 (2018), pp. 3213–3237.

[7] M. A. Chaplain, M. Ganesh, and I. G. Graham, *Spatio-temporal pattern formation on spherical surfaces: numerical simulation and application to solid tumour growth*, Journal of mathematical biology, 42 (2001), pp. 387–423.

[8] W. Chen and M. J. Ward, *The stability and dynamics of localized spot patterns in the two-dimensional Gray–Scott model*, SIAM Journal on Applied Dynamical Systems, 10 (2011), pp. 582–666.

[9] Y. Chen, T. Kolokolnikov, J. Tzou, and C. Gai, *Patterned vegetation, tipping points, and the rate of climate change*, European Journal of Applied Mathematics, 26 (2015), pp. 945–958.

[10] D. Coombs, R. Straube, and M. Ward, *Diffusion on a sphere with localized traps: Mean first passage time, eigenvalue asymptotics, and fekete points*, SIAM Journal on Applied Mathematics, 70 (2009), pp. 302–332.

[11] M. P. Do Carmo, *Differential geometry of curves and surfaces: Revised and updated second edition*, Courier Dover Publications, 2016.

[12] A. Doelman, W. Eckhaus, and T. J. Kaper, *Slowly modulated two-pulse solutions in the Gray–Scott model ii: Geometric theory, bifurcations, and splitting dynamics*, SIAM Journal on Applied Mathematics, 61 (2001), pp. 2036–2062.

[13] A. Doelman, R. A. Gardner, and T. J. Kaper, *Stability analysis of singular patterns in the 1D Gray-Scott model: a matched asymptotics approach*, Physica D: Nonlinear Phenomena, 122 (1998), pp. 1–36.

[14] ———, *A stability index analysis of 1-D patterns of the Gray-Scott model*, American Mathematical Soc., 2002.

[15] A. Doelman, T. J. Kaper, and W. Eckhaus, *Slowly modulated two-pulse solutions in the Gray–Scott model i: Asymptotic construction and stability*, SIAM Journal on Applied Mathematics, 61 (2000), pp. 1080–1102.

[16] A. Doelman, T. J. Kaper, and P. A. Zegeling, *Pattern formation in the 1-d Gray-Scott model*, Nonlinearity, 10 (1997), pp. 523–563.

[17] FlexPDE7, PDE Solutions Inc. URL http://www.pdesolutions.com, (2017).

[18] P. Gandhi, L. Werner, S. Iams, K. Gowda, and M. Silber, *A topographic mechanism for arcing of dryland vegetation bands*, Journal of The Royal Society Interface, 15 (2018), p. 20180508.

[19] E. Gilad, J. von Hardenberg, A. Provenzale, M. Shachak, and E. Meron, *Ecosystem engineers: from pattern formation to habitat creation*, Physical Review Letters, 93 (2004), p. 098105.

[20] K. Gowda, Y. Chen, S. Iams, and M. Silber, *Assessing the robustness of spatial pattern sequences in a dryland vegetation model*, Proceedings of the Royal Society A: Mathematical, Physical and Engineering Sciences, 472 (2016), p. 20150893.

[21] D. Iron, M. J. Ward, and J. Wei, *The stability of spike solutions to the one-dimensional Gierer–Meinhardt model*, Physica D: Nonlinear Phenomena, 150 (2001), pp. 25–62.

[22] C. A. Klausmeier, *Regular and irregular patterns in semiarid vegetation*, Science, 284 (1999), pp. 1826–1828.

[23] T. Kolokolnikov, W. Sun, M. Ward, and J. Wei, *The stability of a stripe for the Gierer–Meinhardt model and the effect of saturation*, SIAM Journal on Applied Dynamical Systems, 5 (2006), pp. 313–363.

[24] T. Kolokolnikov, M. S. Titcombe, and M. J. Ward, *Optimizing the fundamental Neumann eigenvalue for the Laplacian in a domain with small traps*, Europ. J. Appl. Math., 16 (2005), pp. 161–200.

[25] T. Kolokolnikov, M. Ward, J. Tzou, and J. Wei, *Stabilizing a homoclinic stripe*, Philosophical Transactions of the Royal Society A: Mathematical, Physical and Engineering Sciences, 376 (2018), p. 20180110.
[26] T. Kolokolnikov, M. J. Ward, and J. Wei, *The existence and stability of spike equilibria in the one-dimensional Gray–Scott model: The low feed-rate regime*, Studies in Applied Mathematics, 115 (2005), pp. 21–71.
[27] ———, *The existence and stability of spike equilibria in the one-dimensional Gray–Scott model: The pulse-splitting regime*, Physica D: Nonlinear Phenomena, 202 (2005), pp. 258–293.
[28] T. Kolokolnikov, M. J. Ward, and J. Wei, *Spot self-replication and dynamics for the Schnakenberg model in a two-dimensional domain*, J. Nonlinear Sci., 19 (2009), pp. 1–56.
[29] A. L. Krause, A. M. Burton, N. T. Fadai, and R. A. Van Gorder, *Emergent structures in reaction-advection-diffusion systems on a sphere*, Physical Review E, 97 (2018), p. 042215.
[30] A. L. Krause, M. A. Ellis, and R. A. Van Gorder, *Influence of curvature, growth, and anisotropy on the evolution of Turing patterns on growing manifolds*, Bulletin of mathematical biology, 81 (2019), pp. 759–799.
[31] C. Landsberg and A. Voigt, *A multigrid finite element method for reaction-diffusion systems on surfaces*, Computing and visualization in science, 13 (2010), pp. 177–185.
[32] J. M. Lee, *Riemannian manifolds: An introduction to curvature*, vol. 176, Springer Science & Business Media, 2006.
[33] K.-J. Lee, W. D. McCormick, J. E. Pearson, and H. L. Swinney, *Experimental observation of self-replicating spots in a reaction–diffusion system*, Nature, 369 (1994), pp. 215–218.
[34] W. Macfadyen, *Vegetation patterns in the semi-desert plains of british somaliland*, The Geographical Journal, 116 (1950), pp. 199–211.
[35] P. Maini, K. Painter, and H. P. Chau, *Spatial pattern formation in chemical and biological systems*, Journal of the Chemical Society, Faraday Transactions, 93 (1997), pp. 3601–3610.
[36] B. J. Matkowsky, *Nonlinear dynamic stability: a formal theory*, SIAM Journal on Applied Mathematics, 18 (1970), pp. 872–883.
[37] G. S. McGrath, K. Paik, and C. Hinz, *Microtopography alters self-organized vegetation patterns in water-limited ecosystems*, Journal of Geophysical Research: Biogeosciences, 117 (2012).
[38] E. Meron, H. Yizhaq, and E. Gilad, *Localized structures in dryland vegetation: forms and functions*, Chaos: An Interdisciplinary Journal of Nonlinear Science, 17 (2007), p. 037109.
[39] C. B. Muratov and V. Osipov, *Stability of the static spike autosolitons in the gray–scott model*, SIAM Journal on Applied Mathematics, 62 (2002), pp. 1463–1487.
[40] W. Nagata, L. G. Harrison, and S. Wehner, *Reaction-diffusion models of growing plant tips: Bifurcations on hemispheres*, Bulletin of mathematical biology, 65 (2003), pp. 571–607.
[41] J. E. Pearson, *Complex patterns in a simple system*, Science, 261 (1993), pp. 189–192.
[42] M. Rietkerk, M. C. Boerlijst, F. van Langevelde, R. HilleRisLambers, J. v. de Koppel, L. Kumar, H. H. Prins, and A. M. de Roos, *Self-organization of vegetation in arid ecosystems*, The American Naturalist, 160 (2002), pp. 524–530.
[43] M. Rietkerk and J. Van de Koppel, *Regular pattern formation in real ecosystems*, Trends in ecology & evolution, 23 (2008), pp. 169–175.
[44] I. Rozada, S. J. Ruuth, and M. J. Ward, *The stability of localized spot patterns for the Brusselator on the sphere*, SIAM J. Appl. Dyn. Sys., 13 (2014), pp. 564–627.
[45] L. Sewalt and A. Doelman, *Spatially periodic multipulse patterns in a generalized Klausmeier–Gray–Scott model*, SIAM Journal on Applied Dynamical Systems, 16 (2017), pp. 1113–1163.
[46] J. A. Sherratt, *Pattern solutions of the Klausmeier model for banded vegetation in semi-arid environments I*, Nonlinearity, 23 (2010), p. 2657.
[47] ———, *Pattern solutions of the Klausmeier model for banded vegetation in semiarid environments IV: Slowly moving patterns and their stability*, SIAM Journal on Applied Mathematics, 73 (2013), pp. 330–350.
[48] E. Siero, A. Doelman, M. Eppinga, J. D. Rademacher, M. Rietkerk, and K. Siteur, *Striped pattern selection by advective reaction-diffusion systems: Resilience of banded vegetation on slopes*, Chaos: An Interdisciplinary Journal of Nonlinear Science, 25 (2015), p. 036411.
[49] P. H. Trinh and M. J. Ward, *The dynamics of localized spot patterns for reaction-diffusion systems on the sphere*, Nonlinearity, 29 (2016), pp. 766–806.
[50] W. H. Tse, J. Wei, and M. Winter, *The Gierer–Meinhardt system on a compact two-dimensional Riemannian manifold: Interaction of Gaussian curvature and Green's function*, Journal de mathématiques pures et appliquées, 94 (2010), pp. 366–397.
[51] A. M. Turing, *The chemical basis of morphogenesis*, Bulletin of mathematical biology, 52 (1990), pp. 153–197.
[52] J. Tzou and L. Tzou, *Spot patterns of the Schnakenberg reaction-diffusion system on a curved torus*, Nonlinearity, (2019).
[53] J. Tzou, S. Xie, T. Kolokolnikov, and M. J. Ward, *The stability and slow dynamics of localized spot patterns for the 3-D Schnakenberg reaction-diffusion model*, SIAM Journal on Applied Dynamical Systems, 16 (2017), pp. 294–336.
[54] S. van der Stelt, A. Doelman, G. Hek, and J. D. Rademacher, *Rise and fall of periodic patterns for a generalized Klausmeier–Gray–Scott model*, Journal of nonlinear science, 23 (2013), pp. 39–95.
[55] R. A. Van Gorder, V. Klika, and A. L. Krause, *Non-autonomous Turing conditions for reaction-diffusion systems on evolving domains*, arXiv preprint arXiv:1904.09683, (2019).
[56] M. J. Ward, *Asymptotic methods for reaction-diffusion systems: past and present*, Bulletin of mathematical biology, 68 (2006), p. 1151.
[57] M. J. Ward, W. D. Henshaw, and J. B. Keller, *Summing logarithmic expansions for singularly perturbed eigenvalue problems*, SIAM Journal on Applied Mathematics, 53 (1993), pp. 799–828.

[58] M. J. Ward and J. Wei, *The existence and stability of asymmetric spike patterns for the Schnakenberg model*, Studies in Applied Mathematics, 109 (2002), pp. 229–264.
[59] S. Xie and T. Kolokolnikov, *Moving and jumping spot in a two-dimensional reaction–diffusion model*, Nonlinearity, 30 (2017), p. 1536.